Theoretical Performance Model and Initial Experimentation of a Baffled-Tube Ram Accelerator

Jeffrey F. Glusman

A thesis submitted in partial fulfillment of the
requirements for the degree of

Master of Science

University of Washington

2016

Committee:

Carl Knowlen, Chair

Mitsuru Kurosaka

Program Authorized to Offer Degree:
Aeronautics and Astronautics

University of Washington

Abstract

Theoretical Performance Model and Initial Experimentation of a Baffled-Tube Ram Accelerator

Jeffrey F. Glusman

Chair of the Supervisory Committee:
Research Associate Professor Carl Knowlen
Aeronautics and Astronautics

The baffled-tube ram accelerator is an innovation in hypervelocity launch technology that allows the acceleration of axisymmetric projectiles in the velocity range of 500 to 3000 meters per second. This device has the potential to double the thrust performance of the conventional smooth-bore ram accelerator while reducing its minimum starting velocity. The baffled-tube ram accelerator utilizes a series of internal baffles to suppress the forward surge of a combustion driven shock wave, thus enabling operation in propellants having two to three times the energy release of those used with conventional smooth-bore ram accelerators. An experimental and theoretical investigation of this device is currently on-going at the University of Washington. Operation at velocities between 620 and 1220 meters per second has been demonstrated to date. Theoretical modeling indicates that momentum loss due to baffle interactions is a key factor in the baffled-tube ram accelerator, which reduces its performance. Nevertheless, baffled-tube experiments have demonstrated thrusts 30-100% greater than that of a smooth-bore ram accelerator operating at the same fill pressure. The design, modeling, and experimental results from a 38-mm-bore, two-meter-long baffled-tube ram accelerator apparatus are presented.

TABLE OF CONTENTS

Page

LIST OF FIGURES

Figure Number Page

LIST OF TABLES

Table Number Page

GLOSSARY AND VARIABLE LIST

Glossary

BTRA: Baffled-Tube Ram Accelerator

CAD: Computer Aided Design

CFD: Computational Fluid Dynamics

CJ: Chapman-Jouguet

EM: Electromagnetic

FEA: Finite Element Analysis

MFC: Mass Flow Controller

SBRA: Smooth-Bore Ram Accelerator

TCRA: Thermally-Choked Ram Accelerator

UW: University of Washington

Variable List

F: Thrust Force

P: Pressure

A: Area

M: Mach Number

a: Local Sound Speed

ρ: Density

u: Velocity

γ: Ratio of Specific Heats

T: Temperature

R: Specific Gas Constant

h: Enthalpy

Δq: Heat Release

Q: Non-dimensional Heat Release

c_p: Specific Heat at Constant Pressure

r: Radius

I: Non-Dimensional Thrust Force

L: Length

V: Volume

d: Diameter

β: Volume Void Ratio

c_d: Coefficient of Drag

D: Drag Force

n: Integer Number

Φ: Fuel to Air Ratio

x: Axial Distance

t: Time

X: Molar Coefficient

BR: Blockage Ratio

η_Q: Combustion Efficiency

η_β: Void Volume Ratio Efficiency

Subscripts and Superscripts

1: Entrance State

2: Exit (Choke-Plane) State

lab: Lab Frame

i: Initial State

f: Final State

CJ: Chapman-Jouguet State

b: Baffle

p: Projectile

c: Chamber

surf: Surface Area

eff: Effective

CAD: CAD Measured

$*$: Choked Throat

BTRA: Baffled-Tube

SBRA: Smooth-Bore

$\bar{x}$: Average Value of x

$\ddot{x}$: Second-Derivative of x

ACKNOWLEDGMENTS

First and foremost, I would like to thank my adviser, Professor Carl Knowlen, for initially granting me the opportunity to work on the baffled-tube ram accelerator and encouraging me to explore options on optimizing the data reduction process. I sincerely believe that the hours spent working alongside him resulted in lessons learned of gas dynamics, detonations, ram acceleration and most importantly, life. As a member of my reading committee, Professor Mitsuru Kurosaka's inputs and suggestions were crucial in incorporating incomplete combustion and making many key points clearer. Without Professor Arthur T. Mattick and his napkin drawn electronics, entire sections of this work would not have been producible.

To Richard Grist, I don't know where I would have been without your help - you were instrumental in *every* ram accelerator shot and showed me what hard work looked like. Navid Daneshvaran's work in modeling the reacting flow proved to be instrumental insight into the dynamics of the baffled-tube. It would be a shock not to thank Colin Hambling for the work you performed alongside me on the ignition system and in performing the detonation experiments. I wouldn't know the first thing about analyzing data or how to go about resetting the ram if it were not for Tim Elder. Thank you to the graduate students in Guggenheim 307 for putting up with me for two years.

The real MVPs are the undergraduate volunteers who spent more hours than imaginable working to set up and tear down after shots. Specifically, I would like to thank Lucas Heflin for his design work of the baffled-tube, Navi Sanduu for his patience and friendship, Tyler Leis for his hard work and the long hours we spent over

Summer (even though we often didn't see eye-to-eye on musical selection), Charlie Yang and Shray Singh for their machining of projectiles to diaphragms and creation of the ”super mag”, and lastly Greg Derk who kept me sane and often stepped up as help in time of great need.

This work was funded by the Joint Center for Aerospace Technology Innovation (JCATI), EnergeticX and the Washington Research Foundation (WRF): without funding, there would be no baffled-tube ram accelerator, and without a baffled-tube ram accelerator, there would be no data for this thesis.

Lastly, I want to thank my friends and family who think a ram accelerator is used to make mountain goats go really, really fast.

Press on!

Chapter 1

INTRODUCTION

“Nothing in the world can take the place of persistence.”

Calvin Coolidge

In the early 1980’s, researchers at the University of Washington conceived a new method for accelerating micro satellites in direct space launch applications. [1][2] The conventional method of launching satellites involves using a rocket to carry the payload into orbit, thus carrying the fuel and oxidizer along; and hasn’t changed much over the years. Having to store the propellants on board the rocket added significant weight and complexity of the structure and control systems. The novel concept, meant to replace the conventional method, was dubbed the ram accelerator and has been operational as an educational tool for over twenty-five years. [3]

The ram accelerator utilizes a propulsive cycle similar to that of a ramjet engine in which a projectile can be accelerated to near orbital velocities in relatively short distances (Figure 1.1). A conventional ramjet works by moving through the atmosphere at supersonic speeds, ingesting air that is decelerated by a shock train, subsequently mixing in fuel and igniting the mixture to accelerate it out the back end of the engine. A ram accelerator projectile moves supersonically with respect to fixed walls, through a quiescent mixture of fuel and oxidizer in which the shock system of the projectile will initiate the chemical reaction of the propellants causing chemical energy release; therefore accelerating the gases until they reach a state of thermally-choked. [4] As the projectile accelerates, the normal shock moves aft until it falls of the base of the projectile and occupies the tube’s entire cross-sectional area. If the projectile’s base tapered to a point, the velocity of the projectile would be equivalent to the Chapman-Jouguet (CJ) detonation speed when the normal shock just reaches the end of the projectile and ceases thrust production. [3]

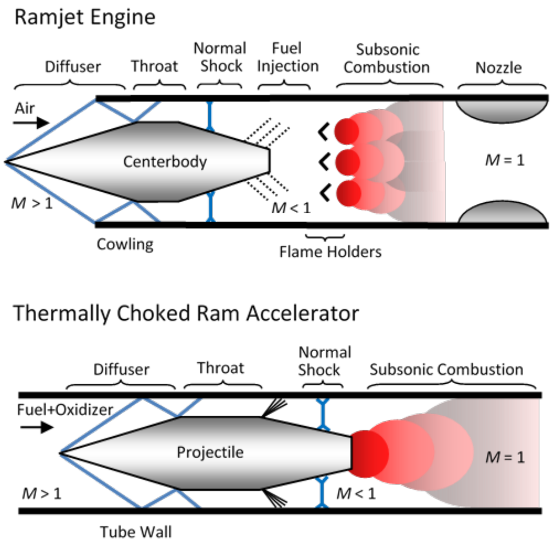

Figure 1.1: Comparison of the conventional air-breathing ramjet to that of the thermally-choked ram accelerator.

Much research has been invested in exploring the operational envelope of the thermally-choked, smooth-bore ram accelerator; which led to understanding two main failure mechanisms that result in unstarting the projectile: minimum entrance Mach number and too energetic propellants. [5][6] The term ’unstart’ is derived from supersonic inlet literature and refers to the disgorging of a normal shock wave from an inlet causing the cessation of supersonic flow through the throat. An unstart is realized when the shock wave reaches the throat of the projectile and is disgorged from the projectile. The aforementioned phenomenon will be thoroughly explained in Chapter 2, as well as the concept of the baffle-tube ram accelerator which extends the operating envelope of the standard thermally-choked model. The theoretical performance model of the baffled-tube ram accelerator will be described as well as how a ram accelerator with arbitrary internal geometry will be compared to the traditional smooth-bore ram accelerator model.

The ram accelerator at the University of Washington is 38-millimeter-bore and is 16-meters-long with the maximum velocity obtained of 2.7 kilometers per second. The technology has been shown to be successfully scale-able through work of the 120-millimeter-bore at the U.S. Army Research Laboratory (ARL) and the 90-millimeter-bore at the French-German Research Institute (ISL). [7][8] The ram accelerator can also be used to control the acceleration profile throughout the experiment by tailoring the mixtures in each section and the overall length of the tube. [9] The UW ram accelerator will be discussed in greater detail in Chapter 3 along with some of the limitations and abilities the facility has.

Chapter 2

DERIVATION OF THEORY

"The power of imagination makes us infinite."

John Muir

In this chapter, two performance models of the baffle-tube ram accelerator will discussed, with groundwork based on the theoretical performance model of the smooth-bore ram accelerator and detonation waves. Problems with the SBRA will be discussed as well as establishing current thoughts on how BTRA will resolve these issues.

2.1 Thermally-Choked Smooth-Bore Ram Accelerator

The thermally-choked, smooth-bore ram accelerator's thrust is uniquely determined by the flow conditions upstream of the projectile as well as at the thermally-choked plane (assuming that the flow is one-dimensional and quasi-steady). The two boundary conditions on a control volume around the projectile, seen in Figure 2.1, are state 1 that is the entrance plane and state 2 that is the exit plane - coinciding with the thermally-choked plane. This is considered a "black-box" model because it ignores the flow phenomenon, such as shock waves, inside the control volume and only takes inputs at states 1 and 2. This is possible because the exit flow is an entropy extremum, therefore the flow processes within the control volume are not significant in the conservation equations of the SBRA. [12]

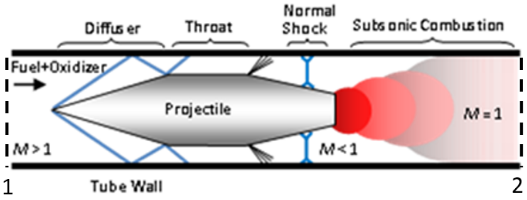

Figure 2.1: Control volume for the "black-box" model of the SBRA.

From conservation of momentum of the above control volume:

$$F = P_2A_2 - P_1A_1 + u_2^2\rho_2A_2 - u_1^2\rho_1A_1$$

noting that A_2 and A_1 are identical can be simplified to A, a non-dimensional thrust parameter can be defined as $\frac{F}{P_1A}$ and using the definition of Mach number ($M = \frac{u}{a}$) simplifying conservation of momentum to:

$$\frac{F}{P_1A} = \frac{P_2}{P_1} - 1 + M_2^2a_2^2\frac{\rho_2}{P_1} - M_1^2a_1^2\frac{\rho_1}{P_1}$$

by using the Ideal Gas Law ($P = \rho RT$) and the equation for local sound speed ($a = \sqrt{\gamma RT}$) this can be simplified further to:

$$\frac{F}{P_1A} = \frac{P_2}{P_1}(1 + \gamma_2M_2^2) - (1 + \gamma_1M_1^2) \tag{2.1}$$

From continuity of the control volume ($\rho_1u_1A_1 = \rho_2u_2A_2$) and same thermodynamic definitions as above:

$$\frac{P_2}{P_1} = \frac{M_1}{M_2}\sqrt{\frac{\gamma_1R_2T_2}{\gamma_2R_1T_1}} \tag{2.2}$$

Conservation of energy on the control volume yields:

$$h_1 + \frac{u_1^2}{2} + \Delta q = h_2 + \frac{u_2^2}{2}$$

by introducing the non-dimensional heat release parameter $Q = \frac{\Delta q}{c_{p1}T_1}$ (where Δq is the heat of reaction, referenced to zero Kelvin) and the thermodynamic properties used prior:

$$\frac{h_1}{c_{p1}T_1} + \frac{\gamma_1 - 1}{2}M_1^2 + Q = \frac{h_2}{c_{p1}T_1} + \frac{\gamma_2 - 1}{2}M_2^2\left(\frac{c_{p2}T_2}{c_{p1}T_1}\right)$$

By solving for the static temperature ratio:

$$\frac{T_2}{T_1} = \frac{c_{p1}}{c_{p2}}\left(\frac{Q + \frac{h_1}{c_{p1}T_1} + \frac{\gamma_1-1}{2}M_1^2}{\frac{h_2}{c_{p2}T_2} + \frac{\gamma_2-1}{2}M_2^2}\right) \tag{2.3}$$

Substituting Equation 2.3 into Equation 2.2, and substituting that result into Equation 2.1 the following relation can be obtained:

$$\frac{F}{P_1A} = \frac{M_1\gamma_1}{M_2\gamma_2}(1+\gamma_2M_2^2)\sqrt{\left(\frac{\gamma_2 - 1}{\gamma_1 - 1}\right)\left(\frac{Q + \frac{h_1}{c_{p1}T_1} + \frac{\gamma_1-1}{2}M_1^2}{\frac{h_2}{c_{p2}T_2} + \frac{\gamma_2-1}{2}M_2^2}\right)} - (1+\gamma_1M_1^2)$$

with the exit plane being thermally-choked, the Mach number is unity, resulting in the final equation of non-dimensional thrust:

$$\frac{F}{P_1A} = M_1\frac{\gamma_1}{\gamma_2}(1+\gamma_2)\sqrt{\left(\frac{\gamma_2 - 1}{\gamma_1 - 1}\right)\left(\frac{Q + \frac{h_1}{c_{p1}T_1} + \frac{\gamma_1-1}{2}M_1^2}{\frac{h_2}{c_{p2}T_2} + \frac{\gamma_2-1}{2}}\right)} - (1+\gamma_1M_1^2) \tag{2.4}$$

The thermal choke plane assumption has been validated by excellent correlation between predicted and experimental values of projectile's accelerations. In practice, this equation is used rarely; a modified version of NASA's Chemical Equilibrium and Applications (CEA) was developed by Depraz [10] to be used to calculate the non-dimensional thrust based on the equilibrium chemistry at state 2. [11] The following plot, Figure 2.2a, which utilizes constant specific heats, $\gamma = 1.4$, shows the effect of M_1 and Q on non-dimensional thrust. As non-dimensional heat release is increased, the resulting non-dimensional thrust increases as well as the zero-thrust Mach number; thus extending the envelope of available performance. Figure 2.2b is a subset, showing a thrust curve for constant values of non-dimensional heat releases $Q = 4$ and $Q = 12$, with constant specific heats. The maximum non-dimensional thrust increases (as well as the corresponding Mach number) and the zero-thrust Mach number (CJ Detonation Mach number) also increases with the increase of Q. It is at the corresponding Mach number of maximum non-dimensional thrust that the lab frame velocity of the choke plane goes to zero.

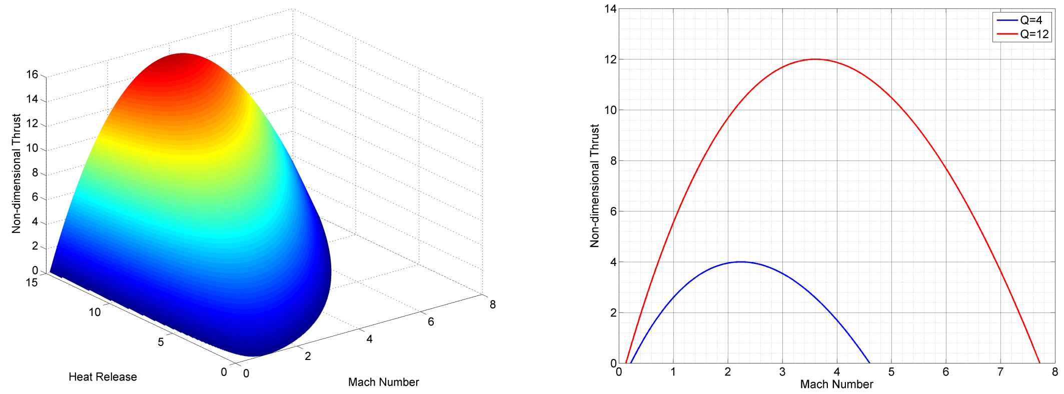

(a) Non-dimensional thrust as a function of incoming Mach number and non-dimensional heat release.

(b) Non-dimensional thrust as a function of incoming Mach number and two values of Q.

Figure 2.2: Non-dimensional thrust for constant values of $\gamma = 1.4$.

2.2 Limitations of SBRA

The analysis above does not predict experimental unstarts of the projectile. Limits of operation were empirically determined in the early days of ram accelerator when testing showed results of a projectile decelerating with a shock wave propagating ahead of it. In order to prevent a high value of Q, the propellants are diluted with combustion products or excessive fuel to lower the heat release ($\mathit{\Delta} q$) to a point where the combustion front would remain on the projectile body. The acceleration and maximum velocity of the projectile in the SBRA are limited by the mixtures non-dimensional heat release, Q, and a minimum

Mach number to achieve at least sonic flow at the throat of the projectile. [14]

Higgins, Knowlen and Bruckner [5] explored two distinct classes of propellants: $2.8CH_4 + 2O_2 + XN_2$ and $2H_2 + 2O_2 + XCH_4$ where X is the molar coefficient and was varied in experiments to better understand the unstart limit due to heat release. X was varied from 3.4 to 12.0 for the methane/oxygen/nitrogen mixture and from 5.0 to 9.0 for the hydrogen/oxygen/methane mixture (Figure 2.3).

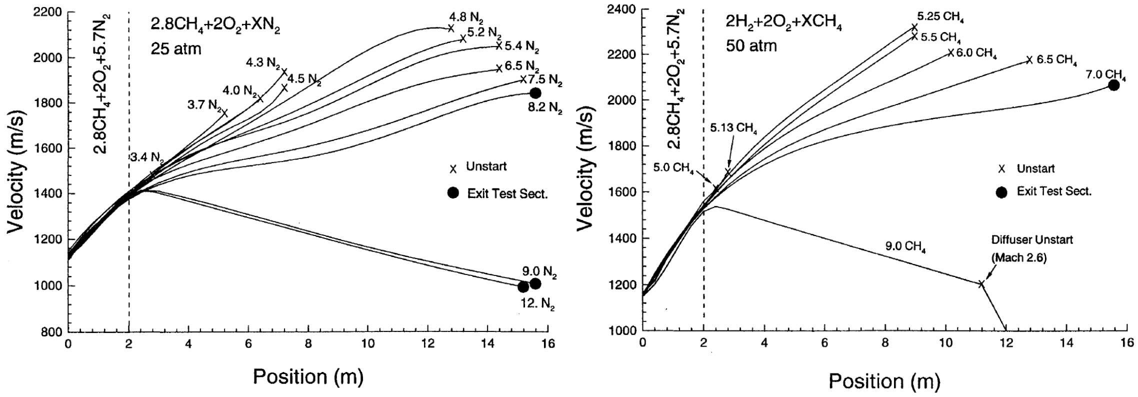

(a) Variable nitrogen dilution, Mach 3.8 transition, $P_1 = 2.5$ MPa.

(b) Variable methane dilution, Mach 3.4 transition, $P_1 = 5.1$ MPa.

Figure 2.3: Velocity - Distance data for varying chemistries and entrance Mach number. [5]

In order to be operating as a ram accelerator, supersonic flow must be sustained at the projectile's largest cross-sectional area. Analytically calculating the geometric conditions, as a function of the incoming Mach number, to sustain a sonic throat requires an iterative procedure as there is not an analytic solution for a supersonic right cone. For approximation purposes, the case of isentropic compression can be used based on the projectile throat diameter, the bore diameter and the flows ratio of specific heats. The relationship can be seen below and areas equated to radii of the bore and projectile:

$$\frac{A}{A^*} = \frac{1}{M}\left(\frac{\frac{\gamma+1}{2}}{1+\frac{\gamma-1}{2}M_1^2}\right)^{\frac{\gamma+1}{2(1-\gamma)}} = \frac{r_b^2}{r_b^2 - r_p^2} \tag{2.5}$$

By this analysis, a 29-millimeter throat projectile in a 38-millimeter-bore would remain supersonic through the throat at a Mach number of approximately 2.4, with $\gamma = 1.4$. This configuration is typical of finned projectiles worked with at UW.

When calculating the limits for a typical finned projectile used at the UW ram accelerator facility, two other scenarios influence the theoretical region of operation. As the non-dimensional heat release is increased, the normal shock is pushed forward on the projectile up unto the limiting condition of a normal shock at the throat of the projectile. The other limit is on the maximum flight Mach number of the projectile; as the projectile's velocity is increased the normal shock is pushed aft until the normal shock is at the base of the projectile. Above that particular Mach number, the projectile no longer follows the thermally-choked model of operation. In the projectile configuration where the aft portion of the projectile tapers to a point, theory predicts the normal shock to be at the tapered point at the CJ detonation velocity. [5] These limits are plotted in Figure 2.4 below.

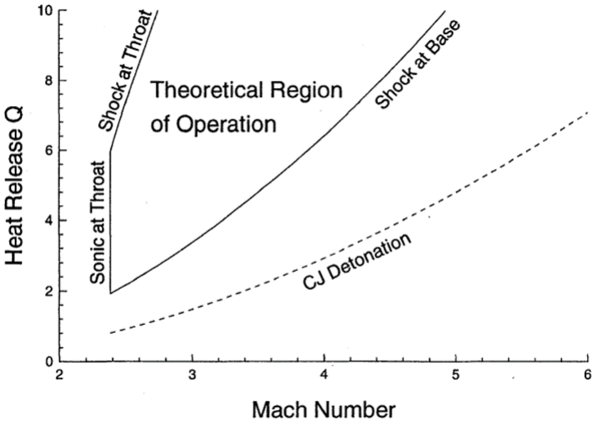

Figure 2.4: Theoretical limits of operation in smooth-bore ram accelerator with typical UW finned projectile. [5]

2.3 Baffle-Tube Ram Accelerator

Dating back to 2005 [13], the baffle-tube ram accelerator has been the newest concept in expanding the operational envelope of the SBRA discussed in the previous section. Baffles, or annular rings, attached to and/or machined into the tube wall are illustrated in Figure 2.5. The concept is best described as a one-way valve preventing the combustion wave surging ahead of the projectile but allowing new propellant to enter and compress. This would allow for mixtures of higher non-dimensional heat release to be used expanding the upper Q range of ram accelerator. Due to the locally larger area ratio the BTRA has a lower entrance Mach number extension to the operational envelope.

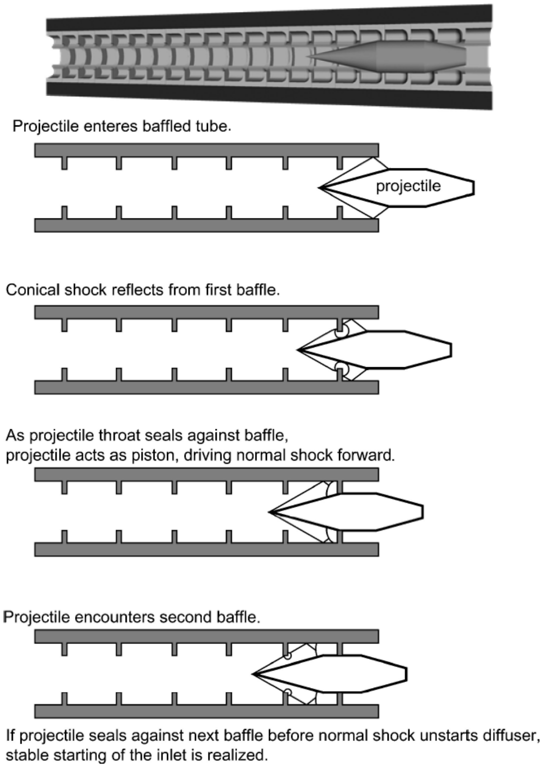

Figure 2.5: Schematic of ram accelerator operation in baffled-tube. [14]

The same analysis can be done for the BTRA minimum entrance Mach number as in the SBRA case in the previous section using Equation 2.5. Based on the ratio of specific heats, chamber diameter (d_c) and the projectiles shoulder diameter, an area ratio can be used to determine the minimum starting Mach number for a given mixture. For a 37-millimeter-bore projectile in a chamber diameter of 76-millimeter, with $\gamma = 1.4$, the minimum Mach number predicted by Equation 2.5 is approximately 1.7. This is a 29% decrease in the necessary Mach number, and corresponding velocity, of a projectile to remain started when compared to a typical SBRA system.

Both expansions of the envelope are caused by the same gas dynamic effects caused by the existence of the baffles. As the projectile approaches the baffle, interaction of the conical shock at the nose and the baffle will drive a normal shock into the gas ahead of the baffle. In the limit of a very thick baffle, this normal shock could be driven far enough ahead to unstart the inlet. Once the throat seals against the baffle, however, the normal shock diffracts as it expands into the chamber defined by the baffle. If the baffles are spaced far enough apart, the projectile's shoulder can overtake the diffracting shock and can "recover" before starting the process over again. [14] The term "recover" is used to describe the condition where the attached bow shock on the nose cone returns to the original status (no diffracted shock interactions).

2.4 Performance Model of the BTRA

When operating a ram accelerator in a tube having complex internal geometry, there is no preferential area reference for thrust normalization (used in Equation 2.4). Thus, for the BTRA a more general non-dimensional thrust definition is used in which net thrust is referenced to an equivalent tube area, A_{eff}, determined by the ratio of the net baffle chamber volume, $V_c + V_b$, to the total length, $L_c + L_b$, of one baffle section, as shown Figure 2.6. Using the value of effective area, the BTRA thrust can be normalized and compared with a non-dimensional thrust of a SBRA based on the same effective area of the baffle bore as follows for an axisymmetric geometry without rails:

$$I_{BTRA} = \frac{F}{P_1 A_{eff}} = \frac{F}{P_1}\frac{(L_c + L_b)}{(V_c + V_b)} = \frac{F}{P_1 A_b}\frac{1 + {}^{L_c}/_{L_b}}{[1 + ({}^{d_c^2}/_{d_b^2})({}^{L_c}/_{L_b})]} = \frac{F}{P_1 A_b \beta} = \frac{I_{SBRA}}{\beta} \qquad (2.6)$$

$$\text{with } \beta = \frac{1 + {}^{L_c}/_{L_b}}{1 + \left({}^{d_c^2}/_{d_b^2}\right)\left({}^{L_c}/_{L_b}\right)}$$

where β accounts for the baffle chamber volume as a function of chamber length, L_c, chamber diameter, d_c, baffle thickness, L_b, and baffle inner diameter, d_b (Figure 2.6). Since $\beta \geq 1$, the greater the value of β, the larger the chamber volume and the more propellant per unit tube length is available to accelerate the projectile. The non-dimensional thrust expression for a SBRA is recovered when $\beta = 1$. Hence, to calculate the ideal BTRA dimensional thrust as a function of M_1, the non-dimensional thrust from Equation 2.4 is multiplied by $P_1 A_b \beta$.

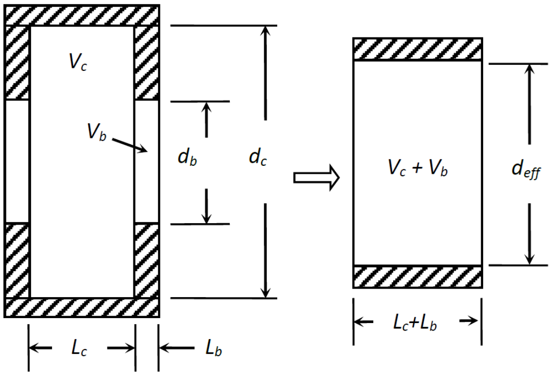

Figure 2.6: Schematic of effective area used for axisymmetric BTRA chamber.

In the case of irregular baffled-tube geometries with rails, a slightly different approach is necessary, which is also applicable to the ideal case shown above. When rails and tapers are present, it is convenient to utilize volume measurements from the 3-D CAD (computer aided design) in order to calculate β. In order to create a general expression, the calculation of β is based only on the diameter of the bore and the chamber diameter (previously defined), the volume (V_{exact}) and length of a single insert (h) and overall length of the baffled-tube section (L); which are all design parameters of the system. As shown previously in Equation 2.6, β can be related to the ratio of the effective tube area and the original tube area. Further, this can be extended into volume because both models use the same length, effectively multiplying this ratio by unity. This allows the writing of the definition of the effective BTRA volume

(V_{eff}) as the volume of a cylinder with the same outer diameter as the insert minus the actual volume predicted from CAD model for the given length of the insert. Specific values of these parameters will be shown in detail in Section 3.2.

$$\beta = \frac{A_{eff}}{A_b} \rightarrow \beta = \frac{V_{eff}}{A_b L} = \frac{\frac{\pi}{4} d_c^2 L - \frac{V_{exact}}{h} L}{A_b L} = \frac{\frac{\pi}{4} d_c^2 - {}^{V_{exact}}\!/_{h}}{A_b} = \frac{\frac{\pi}{4} d_c^2 - {}^{V_{exact}}\!/_{h}}{\frac{\pi}{4} d_b^2}$$

$$I_{BTRA} = \frac{F}{P_1 A_{eff}} = \frac{F}{P_1 A_b \beta} = \frac{I_{SBRA}}{\beta} \tag{2.7}$$

2.5 *Initial Drag Model*

The baffles will cause a drag force as an effect of the gases between the thermally-choked plane and the terminating shock on the aft-body of the projectile moving through the obstacles. The CJ detonation velocity deficit was well defined for some prior experiments that were performed by Lu *et al.* [15] in which the authors measured flame propagation speeds for a fixed blockage ratio ($BR = 1 - [{}^{d}\!/_{D}]^2$) of 0.5 with three obstacle spacing ratios, many hydrocarbon - air mixtures, at various stoichiometries (both fuel-lean and fuel-rich).

The experiments performed by Lu *et al.* were only carried out at atmospheric pressure. Because the BTRA will be operated under higher pressures, experiments were performed in hopes of recreating the data set in the high pressure range of 100 to 450 kPa. The data gathered would be for the specific geometry of the UW baffled-tube geometry at pressures comparable with experimental ram shots through the baffled-tube which are significantly higher than ambient.

The existence of a drag force would change the characteristic of the thrust versus Mach number relation for a given heat release. The following model is introduced to consider a physical value of the drag force within the baffled-tube as a function of the density of the thermally-choked plane, the velocity of the choked plane in the lab frame and the projected area of the baffle:

$$F_{BT,drag} = \frac{1}{2} c_d \rho_2 u_{2,lab}^2 (A_c - A_b) \tag{2.8}$$

$$\text{where, } u_{2,lab} = u_1 - u_2$$

Once this force is non-dimensionalized, as thrust is, it can be subtracted as such from theory. The value of $u_{2,lab}$ is identically zero at the maximum non-dimensional thrust point and increases linearly to the right, and is negative to the left of this point. Therefore, drag acts to decrease performance to the right, resulting in a new maximum Mach number corresponding to zero thrust. Further, performance is increased due to the nature of the "negative drag" value to the left of the zero thrust point. The following plot shows a qualitative representation of this theory based on drag coefficients of 1.0 and 2.0, which are representative values for bluff bodies in subsonic flow.

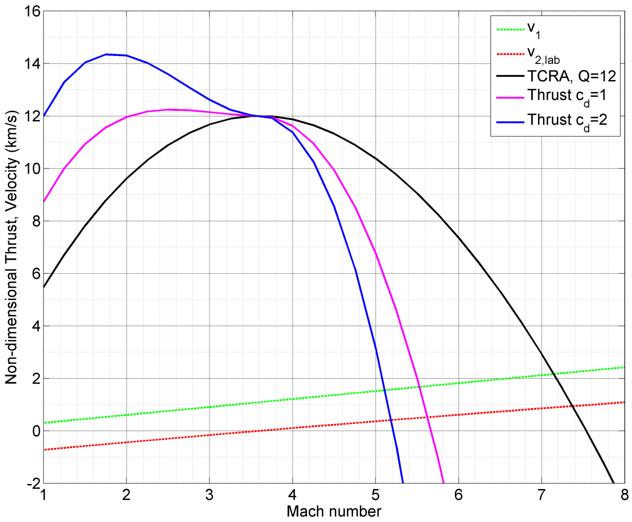

Figure 2.7: Drag Model applied to $Q = 12$ TCRA non-dimensional thrust for two drag coefficients.

Because the drag coefficient is an approximation, an experiment was proposed in hopes of characterizing the drag coefficient of the UW baffled-tube geometry. This will be the main focus of the detonation experiments discussed in later chapters.

2.6 Revised Drag Model

The model previously described in Section 2.5 is incomplete in that it does not take into account the work due to drag/friction in the energy conservation equation. This section will provide the theoretical groundwork for a drag/friction force to be incorporated into the conservation laws described in Section 2.1. In lieu of deriving the non-dimensional thrust equation again, the set of conservation equations will be shown (with the new force, D, incorporated) and then a final solution will be shown and follows the same derivation as before, with the same assumptions (M_2=1) on the same control volume (Figure 2.1). One can notice that a net force could be applied in Equation 2.10 but the thrust, F, does not show up in the energy conservation balance (Equation 2.11). This is because the velocity of the projectile is zero in the control volume reference frame and therefore, no work is done on the flow by this force. [17]

Conservation of mass on the control volume:

$$\rho_1 u_1 A_b = \rho_2 u_2 A_b \tag{2.9}$$

Conservation of momentum on the control volume:

$$P_1 A_b + u_1^2 \rho_1 A_b + F - D = P_2 A_b + u_2^2 \rho_2 A_b \tag{2.10}$$

Conservation of energy on the control volume yields:

$$\rho_1 u_1 A_b \left(h_1 + \frac{u_1^2}{2} + \Delta q \right) - D u_1 = \rho_2 u_2 A_b \left(h_2 + \frac{u_2^2}{2} \right) \tag{2.11}$$

In solving these three simultaneously, the solution is as follows:

$$\frac{F}{P_1 A_b} = M_1 \frac{\gamma_1}{\gamma_2} (1 + \gamma_2) \sqrt{ \left(\frac{\gamma_2 - 1}{\gamma_1 - 1} \right) \left(\frac{Q + \frac{h_1}{c_{p1} T_1} + \frac{\gamma_1 - 1}{2} M_1^2 - \frac{D(\gamma_1 - 1)}{P_1 A_b \gamma_1}}{\frac{h_2}{c_{p2} T_2} + \frac{\gamma_2 - 1}{2}} \right) } - (1 + \gamma_1 M_1^2) - \frac{D}{P_1 A_b} \tag{2.12}$$

The drag force, D, must be calculated, and utilizes specific baffle geometry as well as the effective area described in Section 2.4. The incoming density is chosen as the preferential choice because the exit state requires the chemical equilibrium at each later point to be used for a given incoming Mach number into the thrust equation. The drag force is distributed uniformly from the baffles onto the surface between the baffles. By introducing the baffle projected surface area ($A_{p,b} = 26.84\ \text{cm}^2$) as the surface drag acts upon, the axially wetted area ($A_w = 108.04\ \text{cm}^2$) as the surface area of each chamber (including the outer bore void), the number of chambers effected by combustion ($n_c = 6$ [16]) and the surface area of the control volume of the effective SBRA system (A_{surf}), the following equation for the drag force can be written: [17]

$$D = \frac{1}{2} c_d \rho_1 A_{surf} \frac{A_{p,b}}{A_w n_c} \left| u_1 - u_2 \right| (u_1 - u_2)$$

The effective surface area of the equivalent smooth bore system can be written as a function of the effective area (A_{eff}) and the length of the control volume (L). Luminosity and CFD data both show how the length of the control volume changes with the Mach number of the projectile. [18][19] In this report the length of the control volume will be taken as twice the length of the projectile ($L_p = 17.15$ cm). Further, the definition of A_{eff} can be used to put it in terms of the bore cross sectional area and β:

$$A_{surf} = 2L\sqrt{\pi A_{eff}} = 4L_p\sqrt{\pi A_{eff}} = 4L_p\sqrt{\pi A_b \beta}$$

Thus the drag force can be written in the final form:

$$D = 2 c_d \rho_1 L_p \sqrt{\pi A_b \beta} \frac{A_{p,b}}{A_w n_c} \left| u_1 - u_2 \right| (u_1 - u_2)$$

Upon closer inspection of each of the terms in the drag equations described above, it is clear that they result in geometric dependent variables (β, $A_{p,b}$, A_w and possibly the number of effected chambers, n_c - needs more CFD runs to see how geometry effects the length of the control volume). Therefore, all such terms will be combined into the drag coefficient (c_d) with the exception of the projected area of the baffles and number of chambers that the combustion zone actively effects.

$$D = c_d \rho_1 A_{p,b} n_c \left| u_1 - u_2 \right| (u_1 - u_2) \tag{2.13}$$

With the new drag model above, in the calculation of the revised non-dimensional thrust (Equation 2.12) the figure is plotted with c_d as a parameter. The plot in Figure 2.8 indicates the nominal non-dimensional thrust in black, the revised drag model with $c_d = 0.1$ in red, $c_d = 0.5$ in green and $c_d = 1.0$ in blue.

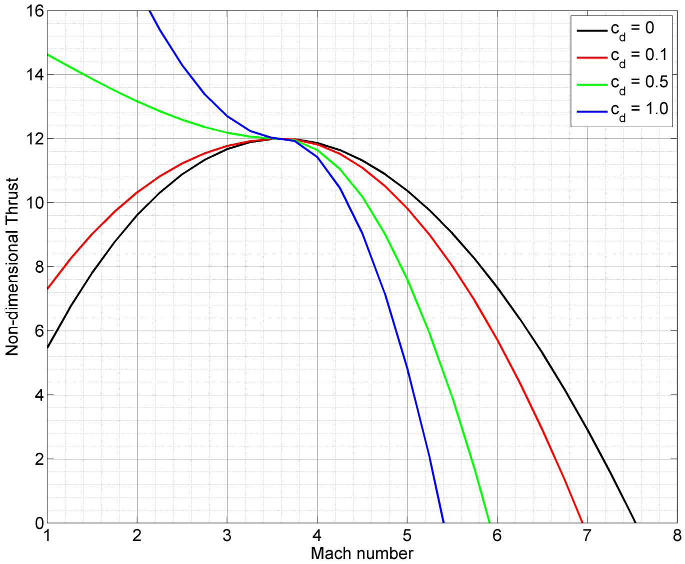

Figure 2.8: Revised Drag Model applied to $Q = 12$ TCRA non-dimensional thrust with various drag coefficient parameter values.

The two drag models are compared in Figure 2.9 with the revised c_d reduced by a factor of 4 from the initial to the revised version. In the Mach number range of 2 to the maximum thrust Mach number, the revised model shows less performance than the initial; however, above the maximum thrust Mach number, the revised model shows less of a deficit than the initial drag model.

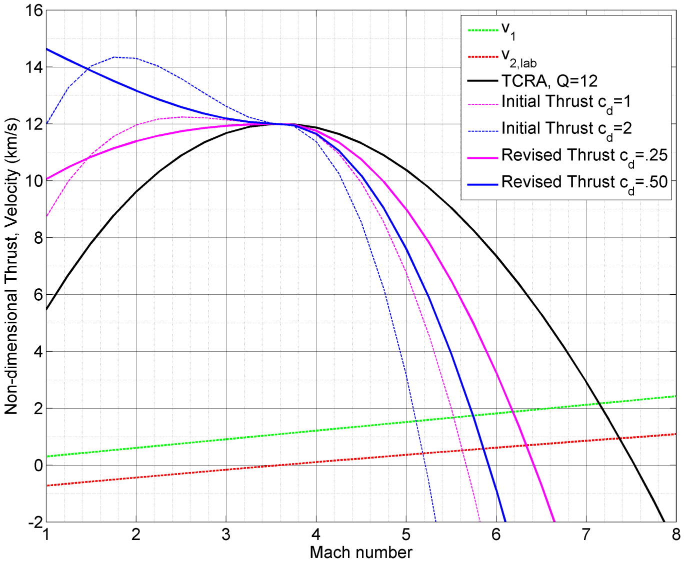

Figure 2.9: Revised Drag Model comparison with Initial Drag Model applied to $Q = 12$ TCRA non-dimensional thrust for two drag coefficients.

Chapter 3

EXPERIMENTAL SETUP AND METHODOLOGY

"Everything should be made as simple as possible, but not simpler."

Albert Einstein

This chapter presents an overview of the laboratory in which all data here within was collected and gives insight into the individual components that worked in concert to achieve reliable, repeatable data. Two major types of experiments were carried out: velocity deficit measurements of detonations propagating through the baffle-tube test section and hot shot testing via ram acceleration through the BTRA.

3.1 Experimental Facility

The ram accelerator facility consists of three main sections: a light gas gun, the ram accelerator test section and the decelerator section. The 38-millimeter-bore, 6-meter-long single-stage gas gun is used to accelerate the projectile to a starting velocity high enough to sustain supersonic flow past the projectile throat. For the BTRA testing, the starting velocities ranged from 600 to 1,100 meters per second which correlate to Mach 2.03 and 3.65, respectively. The ram accelerator section length totals 16-meters, consisting of eight 2-meter-long sections that have a 38-millimeter-bore and 102-millimeter-O.D. The entire system is designed to operate at propellant fill pressures up to 5 MPa.[20] Over the entirety of the test section, there are 40 equidistant instrumentation port stations at 40-centimeter intervals. Each 2-meter-section can be removed and swapped with the BTRA test section. At each of these same joints thin Mylar diaphragms can be used to close off each end and separate different mixtures in multistage experiments. A more in-depth description of the facility can be found in Reference [4]. A schematic of the layout is seen in Figure 3.1a and a typical SBRA projectile drawing is shown in Figure 3.1b.

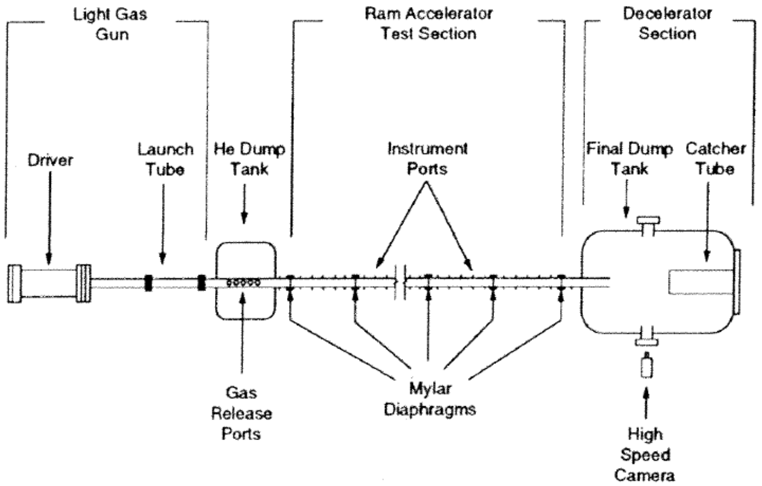

(a) Schematic of University of Washington ram accelerator layout.

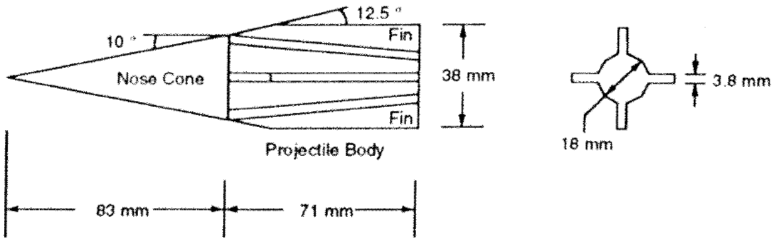

(b) Typical SBRA projectile drawing.

Figure 3.1: Ram accelerator facility and projectile.

The gas handling capabilities of this facility can be found in Reference [21]. The highlights include the use of Brooks Instrument Mass Flow Controllers (MFCs) to control the molar ratios of fuels, oxidants and diluents. The separate gases are metered and mixed in-line through the tubing routing the mixture to the desired segment of the test section. During the course of the experiments a new calibration procedure was developed and verified. The procedure now uses LabVIEW to read the calibration test sections pressure directly and calculates the first and second derivatives of pressure versus time to get ${}^{dP}/_{dt}$ values for a fixed volume (typically that of a 2-meter-long section of SB) at particular set points on the MFCs. For a given chemistry, the desired mole ratios lead to ${}^{dP}\!/_{dt}$ for requirements, and the calibration points are linearly interpolated to calculate the MFC settings of each gas.

The data acquisition system is based on a National Instruments PXIe-1071 configured to collect data from the piezoelectric pressure transducers (PCB 119) and electromagnetic (EM) sensors (of an in-house design [22]) at 1.25 MHz across up to 32 channels. EM sensor data consist of up to 40 separate signals that are multiplexed into 6 of the 32 available channels, allowing up to 26 pressure transducers to be monitored with the remaining data channels. In addition to measuring the tube wall pressure field, the arrival time data obtained by pressure transducers and EM probes at known axial distances along the test section are used to calculate the velocity-distance profiles, from which the thrust-Mach number characteristics can be determined (discussed in Chapter 4).

3.2 Baffled-Tube Design

The primary components of the BTRA system are the baffled inserts which are housed in a 2-meter-shell that integrates into the test section. The benefits of the insert system include the ability to replace the inserts if damaged, test new baffle designs and lower machining costs of the system. The focus of the new design of the baffled-tube inserts was to maintain structural rigidity while maximizing the void volume. The motivation of maximizing the void volume was to increase the amount of propellant available and therefore maximize the performance of the system. An AISI-4140 carbon steel hardened to RC 32-36 was chosen to handle the intense pressure and stresses, inherent in the BTRA system, without yielding ($\sigma_Y \approx 590$ to 690 MPa).

In order to maintain operation, the projectile shoulder length must span at least one baffle chamber; otherwise the system loses the one-way valve effect that the baffled geometry provides. The one-piece axisymmetric projectile is shown in Figure 3.2 where the shoulder is the cylindrical section of greatest cross-sectional area. The aft end of the projectile is to be drilled and tapped such that a Neodymium magnet can be secured in place with a threaded insert. A total of 112 chambers over four-meters was chosen and the final design (Figure 3.3) of the inserts were to consist of eight chambers. This was due to machinability and cost control of the inserts.

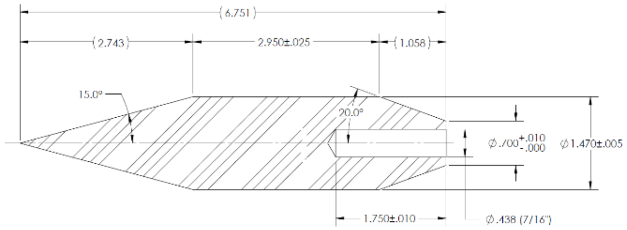

Figure 3.2: Axisymmetric BTRA projectile (drawing in inches).

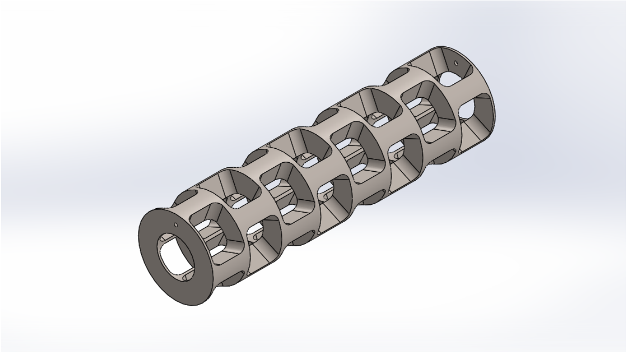

Figure 3.3: 3D CAD model of baffled-tube insert.

A design study for the orientation of the baffle supports was completed by Lucas Heflin before production of the baffled inserts. [23] The existence of the longitudinal rails is to guide the projectile and also add rigidity to the baffled inserts validated in the initial baffled-tube study. [13] ANSYS static structural analysis showed that the offset rail (Figure 3.4c) design was nearly 3 times stronger than the linear rail design (Figure 3.4b) with an average of 250% decrease in maximum equivalent stress on the baffle wall when loaded with 14 MPa on one side (Figure 3.4a). This loading condition represents the highest value expected during operation of the BTRA. The rails were 3.81-millimeters in thickness and were assumed to be fixed supports.

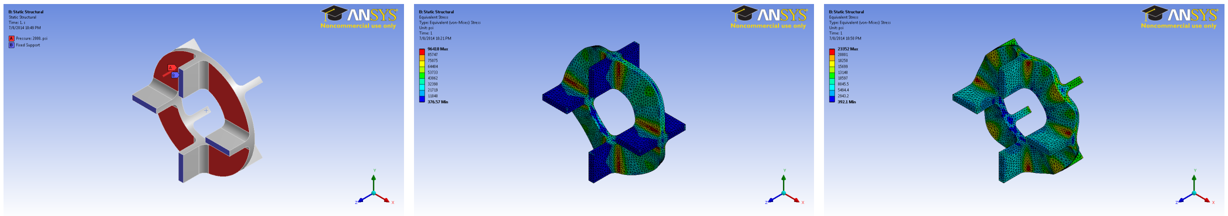

(a) FEA load conditions (b) Linear rail setup (c) 45° offset rail setup

Figure 3.4: Static structural analysis with ANSYS to determine stress concentration with varying rail orientation.

A drawback to the offset rail design is the longitudinal deformation of the baffle sections. Four parallel rails offer excellent rigidity to longitudinal deformation while the offset design enabled the design to be more susceptible to compressive forces and spring-like deformation. However, the main design goal was to maintain structural rigidity of the walls and any compressive forces that would cause the spring-like deformation was estimated to be minimal. Thus, the offset design was preferred. Initial testing proved that the estimation of the minimal spring-like deformation was incorrect, or the single-cell analysis was not adequate to model the subsequent forces on the baffle inserts. These results of the testing will be shown and discussed later in Section 5.2.

Once the offset rail design was chosen, a matrix of varying wall thicknesses and fillet radii was created for the same loading model as in Figure 3.4a. The results for this study are shown below in Table 3.1 in terms of $\sigma_{e,max}$, the maximum localized stress. [23] The wall thickness has a much greater significance on the strength than the filet radius (besides at thin wall thickness). The most important factor in choosing the wall thickness- fillet radius combination is the void space of the baffle. With void space in mind, a wall thickness of 3.81-millimeters and fillet radius of 6.35-millimeters was chosen to achieve sufficient strength and maximize the void space. The ends of each insert had a wall thickness half that of the interior walls such that the spacing was consistent when inserts were joined together.

Table 3.1: $\sigma_{e,max}$ (MPa) from static structural analysis for varying wall thickness and fillet radius

$\sigma_{e,max}$ (MPa)		Fillet Radius (mm)		
		3.175	3.810	6.350
Wall Thickness (mm)	3.175	233.7	206.8	131.0
	3.810	182.7	161.3	125.5
	6.350	121.3	120.0	111.0

Four variations for the rail shape were considered: a linear rail (Figure 3.4), a pie cut rail (Figure 3.5a), a tapered cut rail (Figure 3.5b) and an exponential power-law cut rail (Figure 3.5c). The baffled-tube design of 2005 used the linear rail due to the simplicity in manufacturing and was validated via experimentation. However, the next generation insert was to maximize the void space and minimize the stress concentration factor. The pie cut rail uses a taper, beginning at the center of the bore, such that the taper angle is equal to the angle spanned from the centerline of the insert. The tapered rail is a 20° taper beginning slightly inside of the inner diameter, such that the initial arclength begins at 2.54-millimeters and ends at 15.875-millimeters at the outer edge. The power-law rail has the same arc lengths as the tapered rail but the shape between is governed by an exponential equation. The same load condition of 14 MPa with the same boundary conditions was applied with deformations seen in Figure 3.5 and results in Table 3.2.

Table 3.2: Resulting stress and geometric quantities from static structural analysis for varying rail geometry.

	Pie	Tapered	Power-Law
$\sigma_{e,max}$ (MPa)	80.3	47.0	80.3
K	5.8	3.4	5.8
V_{void} / cm (cm^3/cm)	25.6	23.2	25.7

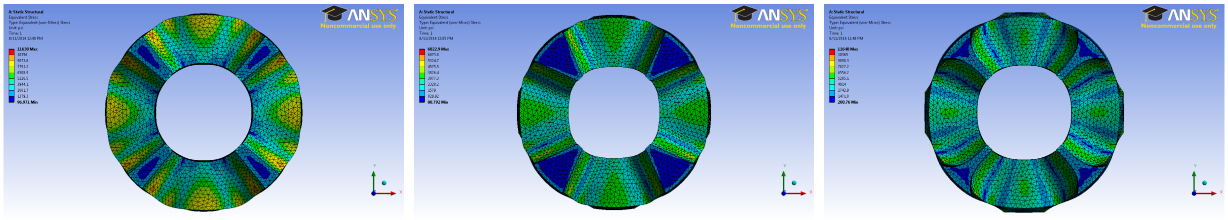

(a) Pie Rail (b) Tapered Rail (c) Power-Law Rail

Figure 3.5: Static structural analysis with ANSYS to determine stress concentration with varying rail shapes.

The linear rails, used in Figure 3.4, were not considered in the above analysis. From the three analyzed, the tapered rail has nearly half the stress concentration factor and only a slight loss in voided volume per length. Further, the tapered rail was feasible to machine and therefore chosen for manufacturing.

The design calls for a 45° offset and therefore requires pins to align the inserts for a continuous pattern of rails for the entire length of the baffle inserts. The initial design relied on small alignment pins and a slide fit, but after reassessment was replaced with four bolted joints with tight axial-location tolerances. The following are the engineering drawing and 3-D CAD model of the initial baffle insert with important parameters listed in Table 3.3.

Table 3.3: Baffle insert geometry and calculated β value.

Chamber Diameter (d_c)	7.590 cm
Baffle Diameter (d_b)	3.815 cm
Insert Length (η)	28.571 cm
CAD Volume (V_{exact})	302.18 cm^3
β	3.009

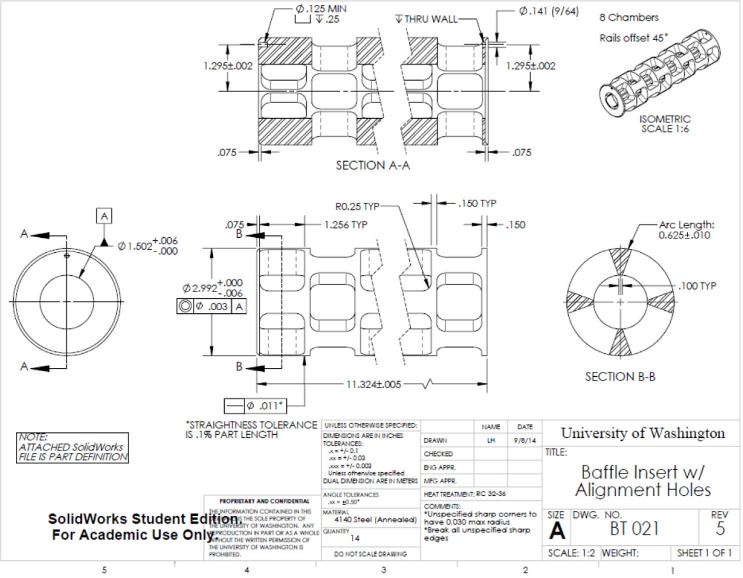

Figure 3.6: Engineering drawing of baffled-tube insert.

The final machined insert can be seen in Figure 3.7 showing the condition of the inserts upon arrival. The fit of the inserts into the outer shell is also shown to illustrate the sliding fit between the inserts and shell.


(a) Manufactured baffled-tube insert.

(b) Insert located within outer shell.

Figure 3.7: Machined inserts and test fit upon arrival at UW Ram Accelerator Facility.

3.3 Baffled-Tube System Integration

The baffled-tube inserts were designed to be a non-interference fit with the outer shell of the baffled-tube. In the design for 4-meters of BTRA, the inserts were slid into each of the outer shells with 7 inserts in each tube. One chamber would stick out of the 55 chamber tube (shown in orange in Figure 3.8) and a joining, instrumented, spacer (shown in cyan) would link the 56 chamber tube (shown in red) and 55 chamber tube. End caps (shown in green) would compress the baffled-tube inserts against the interior seals of the end caps and spacer. In order to insure pressure tight seals at the insert, large flanges (shown in dark blue) were screwed onto the system and bolted together. These same flanges are threaded on the outside of the system and are used to secure the smooth-bore system to the baffled-tube system. Each tube has 5 pairs of instrumentation ports evenly distributed down the length of the tube which are designed to correspond to the center of the baffle chamber volume. A fill port is located at the halfway points in each of the tubes at an open baffle to prevent inhibited flow of propellants into the test section.

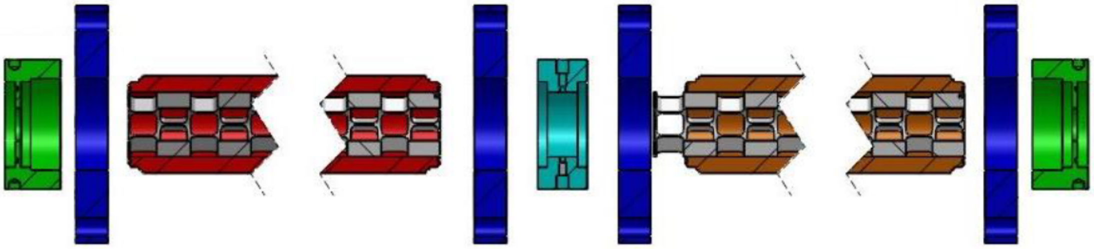

Figure 3.8: Explosion model of the baffled-tube assembly.

In total, fourteen baffled inserts were produced in addition to the two tube shells, tube spacer, two end caps and four flanges. The following photographs are of the machined parts ready for their initial assembly. For preliminary testing only two meters of baffled-tube were assembled and secured into the ram accelerator facility (Figure 3.10).

Figure 3.9: 2-meter section with associated flanges, end caps, and baffled inserts; end view of 2-meter tube with finned projectile for reference.

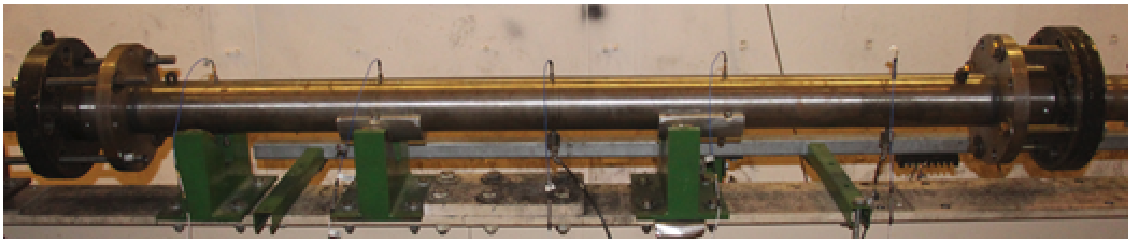

Figure 3.10: 2-meter baffled-tube section installed into UW ram accelerator.

Upon initial testing, deformation of the inserts was observed after a projectile became lodged in the section during an experiment. When the baffle inserts were removed, yielding and localized failure were found in the predicted high stress locations from FEA. It is believed that the axial forces on the baffles were much higher than anticipated leading to deformations in the downstream baffles. Note, these issues were addressed and remedied. The length of the inserts lessened allowing the inserts to accelerate with respect to the tube walls causing even greater forces to be applied, ultimately ending in the failure seen in Figure 3.11. To continue testing, it was necessary to cut the inserts and ensure perpendicularity of the end faces with respect to the bore diameter. Now instead of seven 8-chambered inserts, seven 6-chambered and one 7-chambered inserts are used and each joint is twice a baffle thickness. The joints were drilled and tapped such that they are now bolted together with eight socket cap screws.

While this strengthened the system as a whole, the instrumentation ports were no longer at the center of each baffle, some even completely covered. With the system no longer at the design condition, EM and pressure probes were no longer useful at all instrument stations within the baffled-tube. After each experiment, the length of the assembled baffled-tube inserts is inspected to ensure any yielding is measured and counter-measures are performed (using Mylar diaphragms at either end to ensure a tight fit).

(a) Yielded inserts with localized failure; projectile broken in half and stuck.

(b) Failed baffled at downstream end.

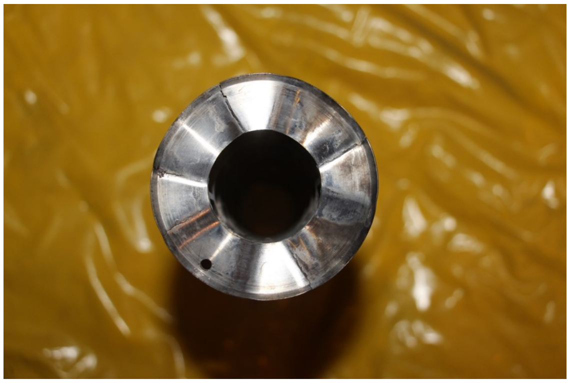

(c) Head on view of failed insert showing failure points, comparable to FEA model.

Figure 3.11: Multiple views of the failed baffled-tube inserts.

A non-reactive CFD analysis performed on arbitrary baffles shows the deviation of the pressure throughout a single baffle thus confirming the unreliable nature of the signals once the inserts had yielded from their design condition. [24] Figure 3.12b indicates the axial position of where a shock would hit the outer wall (where pressure transducers are located). Based on transducers being in different locations in the baffle, significant deviation occurs in when each location "sees" the shock wave, therefore resulting in skewed times and pressure signatures.

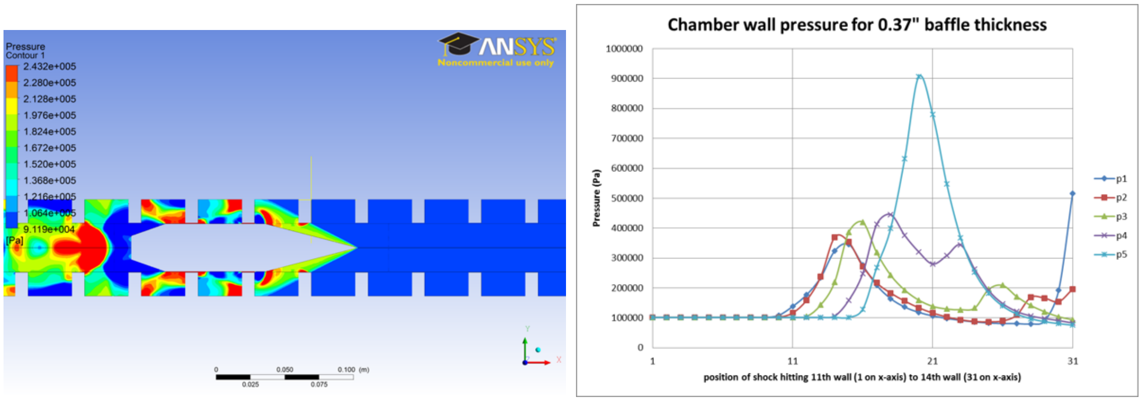

(a) CFD image of static pressure.

(b) Plots of pressure signals at different locations within a baffle.

Figure 3.12: Non-reactive computation fluid dynamic results for 0.37" thick baffles

3.4 Velocity Deficit Measurements

The goal of the velocity deficit experiment was to obtain an experimental point of the velocity deficit of a CJ detonation that would be used in the revised drag model to experimentally determine the value of c_d. In order to test the detonation velocity deficit through the baffled-tube, it would be necessary to form a detonation front in the mixture. This process has been done in the past using a spark plug, a coil and a voltage source; however, the only equipment available was no longer functioning. A few experiments were carried out using a motorcycle's magneto as the voltage source for an automotive spark plug. The goal was to reach approximately 1.4 MPa gauge fill pressures at various stoichiometries. The magneto was tested in methane-oxygen mixture at fuel equivalence ratio (Φ) of $\Phi = 1$ and gauge pressures from 0 to 207 kPa. Due to the fact that the sparking was not occurring at the desired pressures (maximum successful detonation was at 207 kPa), a new spark system was design with the help of Professor Mattick. The schematic of the new spark system can be found in Appendix A along with an installation photo of the spark plug and adapter into the test section. The maximum pressure that the newly design spark system was tested at was approximately 350 kPa in methane-oxygen ($\Phi = 1$) and methane-nitrous oxide mixtures at Φ ranging from 1 to 2, with no detonation found above Φ=1.5. It was not necessary to pursue pressures higher than 350 kPa, for reasons which will be discussed in Section 5.1, therefore a maximum limit to the sparking capabilities was not determined.

For the velocity deficit experiments, only pressure transducers were utilized as EM sensors did not detect shock wave passage well enough to be useful. The experiment began with only 6-meters filled with propellant; a thick, steel diaphragm at the beginning of 2-meters of smooth-bore tube followed by 2-meters of baffled-tube, and two more meters of smooth-bore where a Mylar diaphragm separated the test section and the rest of the apparatus (at vacuum). This experimental setup can be seen in Figure 3.13, below. Initial experiments had pressure transducers installed in 13 out of the 15 instrumentation stations. Later experiments included an additional 2-meters of smooth-bore at the end to allow for a steady state velocity to be measured more confidently and consisted of 17 out of 20 possible pressure probe locations.

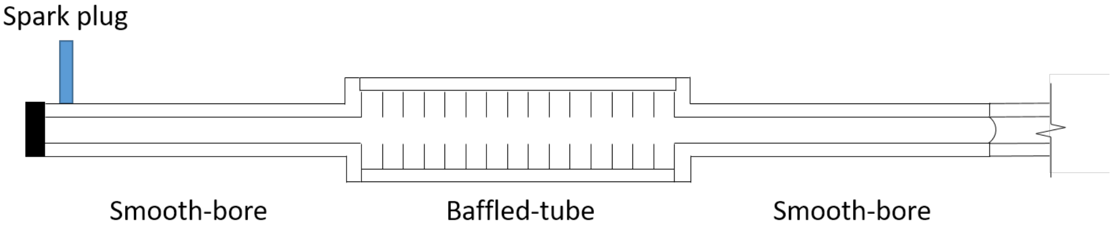

Figure 3.13: Schematic of experimental setup for detonation experiment.

The procedure for the detonation experiments began with installing/validating that all diaphragms were placed in the correct location and pressure checking the test section. Once the MFCs were programmed for a specific stoichiometric ratio of gases, the gases were set to flow until all settings equilibrated sufficiently. During the filling step, pressure downstream of the MFCs were recorded as well as their settings, the time of the fill and final gauge pressure were also recorded. Once the desired fill pressure was reached, all gauges were isolated from the system, vacuum pumps turned off, and the data system would be set to record the experiment's data. Once all personnel and systems were ready, the spark system was initiated. If successfully detonated a distinct *"tink"* was heard and detonation was validated by looking at the gauge pressure of the test section. Detonation were confirmed when the test sections gauge pressure read as vacuum, as the detonation would break the downstream diaphragm and would bring the entire system below ambient. In the event that a detonation did not take place upon firing the spark, another attempt would be made to detonate the mixture after isolating all gauges and validating the data system was ready. If the experiment failed to detonate again, the pressure of the test section would be lowered and tested again; this process repeated until the mixture detonated or reached ambient pressure. In the rare event that an ambient mixture did not detonate, the test section was flooded with nitrogen and brought back to ambient before the vacuum would be utilized to clear the section.

The data analysis of the detonation experiments will be discussed in Section 4.2. A listing of all associated parameters can be found in Appendix C.

3.5 Baffle-Tube Ram Acceleration Shots

The procedure during a baffled-tube ram shot is generally similar to the detonation procedure, except measurements are taken prior to account for the projectile. A Neodymium magnet is carried on-board the projectile and held in place with a threaded insert. Data for the projectiles mass, throat diameter, and shoulder length are recorded as well as the mass, thickness and diameter of the obturator. Once the projectile is adhered to the obturator the mass is measured and recorded, it is then loaded into the launch section immediately downstream of the breech of the light gas gun. Typically two aluminum diaphragms are used to contain the pressure in the light gas gun. These are scribed at specific pressures to regulate the pressure differential in which they burst and allow them to open as consistently as possible. Mylar diaphragms (0.014" thick) are used to separate vacuum sections from the test section and subsequent sections (either vacuum or a high pressure fill of N_2 or CO_2) to slow down the projectile before reaching the catcher tube. The catcher tube is filled with a mix of carpet and metal plates to absorb as much of the kinetic energy of the projectile as possible. At the rear of the breech is a viscous damper to absorb the recoil of the system.

Before each shot the test section is pressure checked to confirm there are not large leaks or poorly secured tubes. After confirming continuity of all pressure transducers, a test of the trigger system is performed with an external magnet through an EM probe hooked directly into the data system. The unexcited outputs of the multiplexed EM probes are also checked to confirm that there are no sporadic signal spikes that could cause the data system to trigger. Continuity is confirmed between the pressure signal smoothing box and the impedance converters attached to each pressure transducer via a built in analog switch.

Two classes of propellants were considered for BTRA: methane-oxygen-carbon dioxide and methane-nitrous oxide. Stoichiometric methane and oxygen ($Q = 16.75$) were diluted with variable carbon dioxide to vary the non-dimensional heat release parameter to the range of 9.0 to 12.5. The gauge fill pressure ranged from 0.93 to 2.10 MPa. The methane-nitrous oxide mixture consisted of one test at Φ=1.5 but was primarily tested at Φ=2, which had an average $Q = 13.05$ for gauge fill pressures ranging from 0.93 to 1.40 MPa.

One and two-piece projectiles were designed for testing in the BTRA. After initial testing of the two-piece projectiles, it was observed that the plastic threaded rod in which held the sections together would fail, resulting in potentially unreliable data. The rod was replaced with a much heavier one (aluminum) and still failed during the shots. Therefore a one-piece projectile was designed which was much stronger but was significantly more massive. The aft boat tail angle was nominally 9° with respect to the projectile shoulder, which was later increased to 12°.

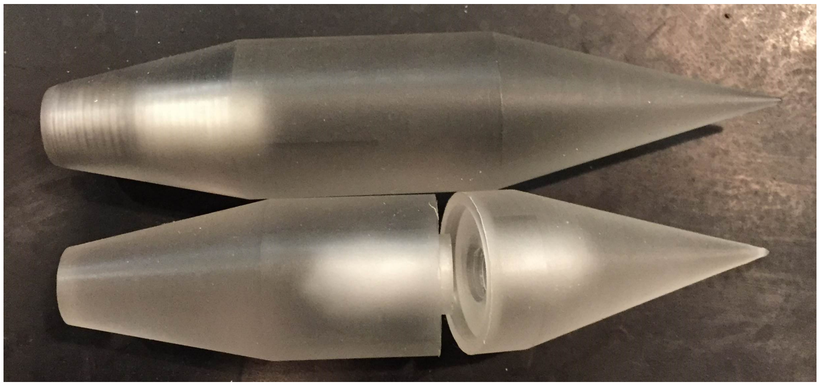

Figure 3.14: Comparison photo of one and two-piece projectiles with 12° aft tail angle.

The data analysis of the baffled-tube ram experiments will be discussed in Section 4.3. A listing of all associated parameters can be found in Appendix E.

Chapter 4

DATA ANALYSIS

"A good engineer is a lazy engineer, but a lazy engineer is not necessarily a good engineer."

Jason Steiner

Within this chapter, discussion of the raw data, how it is processed and presented, and the associated uncertainty will be discussed. The MATLAB code associated with plotting the data set can be found in Appendix B.

4.1 General Data Reduction Technique and Uncertainty

The velocity and acceleration of the projectile at any point in the ram accelerator tube are determined from the time-distance (t-x) data generated by the EM sensors and verified with the pressure transducers. Experimental mean projectile velocities are determined from the central difference of the raw t-x data. This results in an approximation to the velocity at a point midway between the instruments used in the calculation for both sets of probes independently. The maximum uncertainty in the experimentally determined mean projectile velocity is given by the sum of the uncertainties in measuring the separation distance between sensors and the transit time. The maximum relative uncertainty in knowing the separation distances between stations is ∼0.5%. The relative uncertainty in measuring the transit time between transducers is proportional to the projectile velocity and is due primarily to a finite sampling rate and random signal distortions. Analog signals are digitized at a sample rate of 1.25 MHz, which contributes to a maximum uncertainly level of ∼0.4 µs in the measurement of the arrival time of the projectile at any instrumentation station.

A more serious factor limiting the time resolution of the projectile history during an experiment is the distortion of the EM sensor signal itself. Shown in Figure 4.1 are the outputs from four different EM sensors located at the same instrument station. Signals are time synchronized and all are displayed on the same vertical scale (500 mV/div). Each major division on the horizontal scale indicate a 20 µs time interval. Ideally, the time-of-passage of the center of the magnet is determined from the intersection of the line-of-symmetry of the signal with the time axis. Interpretation of the asymmetric and distorted signals is not always so straightforward. Normal procedure is to take the time nearest the midpoint of the ascending signal (or descending if the polarity of the magnet is reversed) as the time-of-passage. The times of projectile magnet passage (relative to the trigger time) taken from the EM signals shown are: 4.138, 4.137, 4.137, and 4.136 ms, from the upper trace to the lower trace, respectively.

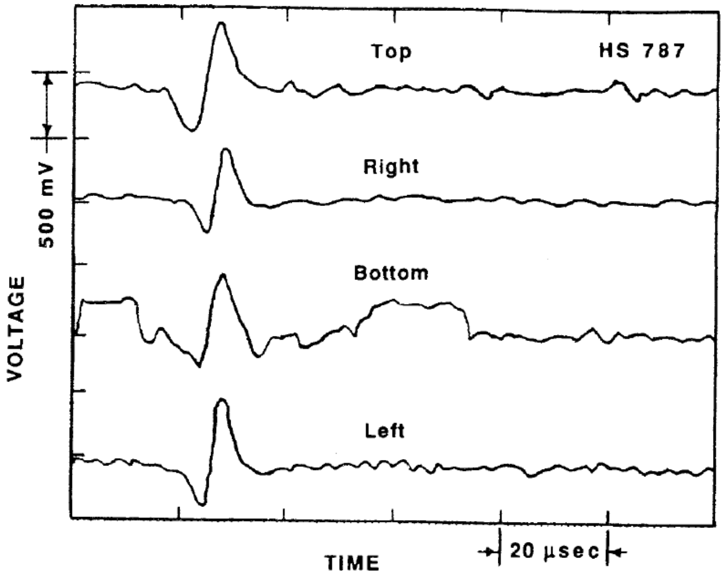

Figure 4.1: Experimental data from coaxial EM senors about a single station. [11]

Additional complications in interpreting the EM signals arise from the shielding effects of the electrically conducting probe casing (316 stainless steel). The diffusion of the magnetic field through the protective casing delays the true signals and results in a slight phase shift which displaces their lines of symmetry. [22][25] However, since all the probes are of uniform construction and the projectile does not change velocity between adjacent instrument stations at an extreme rate, the accuracy of the mean velocity determined from the output of adjacent probes is not affected seriously by differences in this small lag time. (Experiments have shown this phase shift to be ∼2 µs at projectile velocities of ∼1500 meters per second. [22])

The EM data shown in Figure 4.1 are representative of the variations in signal quality that are observed during routine experiments conducted in the current ram accelerator facility. The maximum discrepancy in determining the time-of-passage of the projectile between these signals is 2 µs, which accounts for the digitizing limitations of the DAS and the typical level of signal distortions. Thus the overall uncertainty in measuring the transit time ($\varDelta t$) between any two EM stations is ∼4 µs. The linear relationship of the relative uncertainty, due to measurement errors, for the experimentally determined mean velocity ($\bar{u}$) is as follows:

$$\frac{\varDelta \bar{u}_{EM}}{\bar{u}} = \frac{\varDelta x}{\bar{x}} + \frac{\varDelta t}{\bar{x}}\bar{u} \tag{4.1}$$

where $\varDelta x$ is the uncertainty in the measurement of the separation distance between adjacent instrument stations and $\bar{x}$ is the nominal instrument spacing.

For an accelerating projectile, the mean velocities will always under-predict the actual projectile velocity at the midpoint. The magnitude of the relative velocity error resulting from ignoring the effects of the acceleration on the velocity-distance ($\bar{u}$-x) profile of an experiment is related to projectile velocity as follows:

$$\frac{\varDelta u_{\ddot{x}}}{\bar{u}} = \sqrt{1 + \left(\frac{\ddot{x}_o \bar{x}}{2\bar{u}^2}\right)^2} - 1 \tag{4.2}$$

where $\ddot{x}_o$ is the average acceleration between sensors. A plot of the relative mean velocity error resulting from ignoring acceleration is shown in Figure 4.2, for a projectile undergoing a steady acceleration of $\ddot{x}_o = 50{,}000$ g through a tube having a uniform instrument spacing of $\bar{x} = 40$ centimeters. Note that the effects of acceleration on the experimental mean velocity, at projectile velocities above 1000 meters per second, results in relative mean velocity errors much less than 0.5%.

The total relative uncertainty in the mean velocity measurements of the experiments is the sum of errors given by Equations 4.1 and 4.2. For an experimental uncertainty in instrument spacing of $\Delta x = 1$ millimeter, the variation of the total relative uncertainty in mean velocity, determined with the previously mentioned instrumentation spacing and acceleration conditions is shown in Figure 4.2 for the velocity range of 500 - 2000 meters per second. Since the uncertainty resulting from ignoring accelerations up to 50,000 g is much smaller than the uncertainty in measuring the mean velocity, the $\bar{u} - x$ history of the projectile, determined from the first center differences of the raw t-x data, is not significantly distorted by the typical accelerations of 15,000 to 30,000 g experienced in the current experiments. Thus, the actual projectile velocity at the midpoints between adjacent stations is adequately represented, within the bounds of the measuring uncertainty, by the experimental mean velocity. [11]

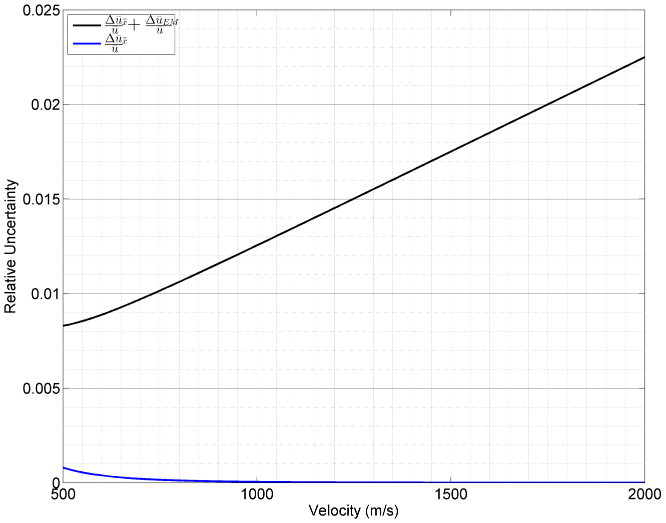

Figure 4.2: Relative uncertainty in velocity and acceleration measurements.

The MATLAB code used to visualize the raw pressure and EM signal outputs can be found in Appendix B.1.

4.2 Velocity Deficit Data Reduction

For the velocity deficit experiments, pressure transducers were relied on for the time of arrival of the detonation wave due to the absence of a projectile and magnet. Figure 4.3 shows the pressure traces at various stations throughout the experimental test section. All four traces indicate an event at 10 ms which corresponds to electrical noise from the high voltage ignition system; this ”noise” serves as the trigger for the run. Because the spark plug is inserted into station 1, the pressure trace is that of the combustion activity as it initiates a deflagration to detonation process that leads to CJ wave formation within one-meter of the spark plug (Figure 4.3a). Station 5 is the last station before the baffled-tube and serves as the last time-of-arrival before entering the BT section. As presented in Figure 4.3c, the signal inside of the baffled-tube is unclear of a particular time-of-arrival and is inconsistent due to the nature of the yielded baffle inserts. Further, the transducer is no longer located at a uniform location in the baffle chamber making the reflections irregular compared to other ports in the baffled-tube. The pressure trace at station 11 (Figure 4.3d) is the first instrumentation port in the second set of smooth-bore and shows a crisp detonation wave that is very similar to that at station 5. A secondary pulse can be seen in the signals for stations 5 and 11 at roughly 14 and 16 ms, respectively, which is attributed to a reflection of the detonation off of the thick metal diaphragm separating the test section from the launch tube.

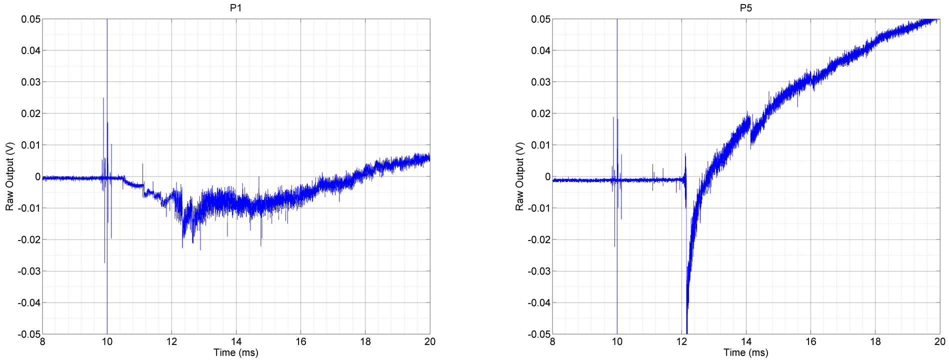

(a) Pressure signal at station 1 (SB). (b) Pressure signal at station 5 (SB).

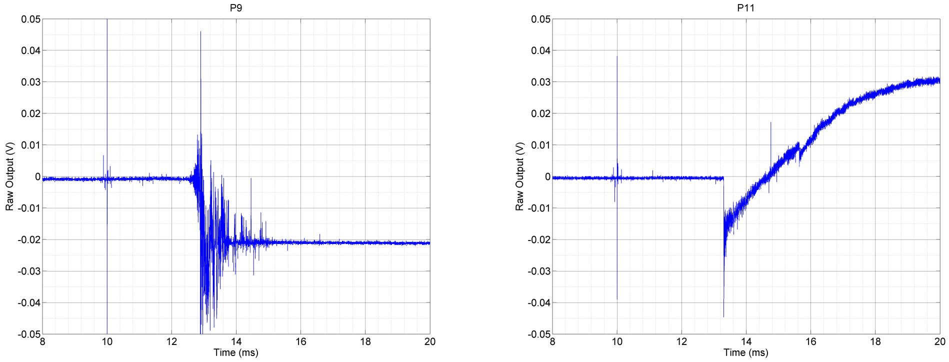

(c) Pressure signal at station 9 (BT). (d) Pressure signal at station 11 (SB).

Figure 4.3: Time synchronized pressure traces for BTD02 at various locations.

In order to view the detonation phenomena more clearly, the pressure traces at stations 5 and 9 have been recreated in Figure 4.4 to show higher fidelity in time. Clear differences are noticeable between the smooth-bore and baffled-tube pressure responses. Figure 4.4a shows a distinct pressure event at approximately 12.15 ms followed by a slow recovery of pressure. Within the baffled-tube, shown in Figure 4.4b, shows a similar pressure event at approximately 12.89 ms but lacks the similar recovery event and instead indicates reflections between the baffles.

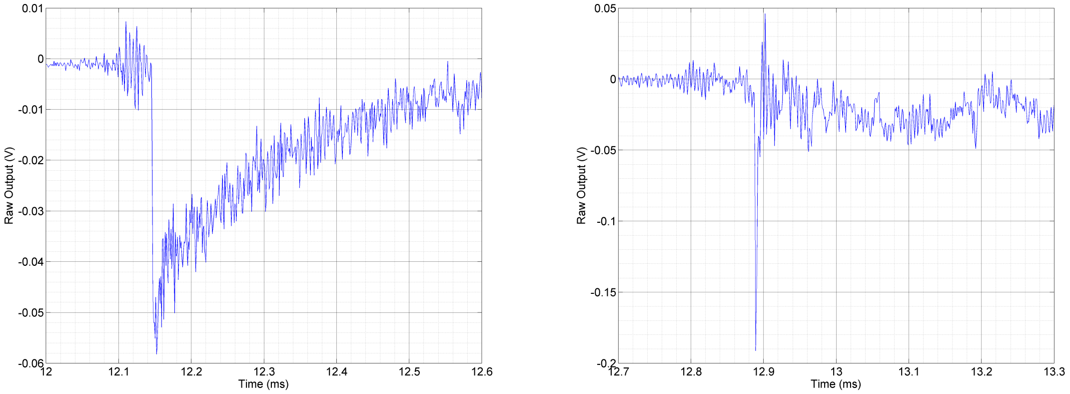

(a) Focused pressure signal at station 5 (SB).

(b) Focused pressure signal at station 9 (BT).

Figure 4.4: Pressure signals focused around first pressure event.

4.2.1 Velocity-Distance Plots for Velocity Deficit Experiment

The signal in the baffled-tube is typically full of reflections and inconsistent due to baffled-tube yielding, therefore the mean velocities through the baffled-tube are calculated based upon the times at stations 5 and 11 in addition to the finite differences at the five stations within the BT (when signals were not irregular). Figure 4.5 incorporates the mean velocities at various locations in the SB and BT sections based on finite differences, as well as where the BT section begins and ends. It also indicates the CJ detonation velocity as calculated by CEA for the given mixture and fill pressure as well as the centered average velocity calculated by the transducers just before and aft of the BT. The deficit is the difference in the local velocity to that of the CJ detonation velocity.

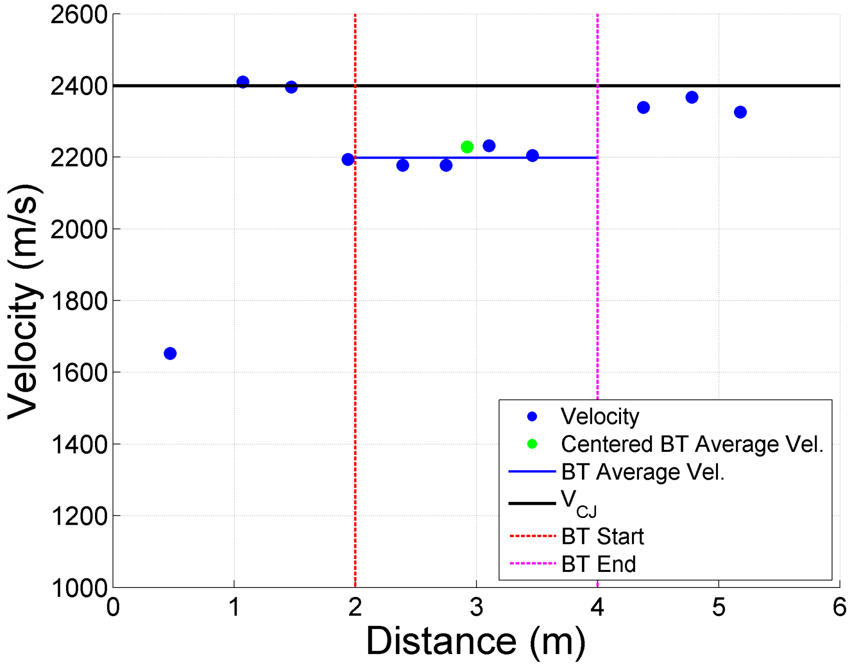

Figure 4.5: Velocity-distance plot for BTD03

The MATLAB code used to plot the velocity-distance diagrams of the velocity deficit experiments can be found in Appendix B.2. Appendix C and Appendix D are the test logs and collection of velocity-distance plots created during testing, respectively.

4.3 Baffle-Tube Data Reduction

For the BTRA testing, both EM probes and pressure transducers were utilized to get two sets of reliable data for calculating the velocities of the projectile and associated shocks. The EM data tracks the projectile while the pressure transducers track the lead shock wave. In the case of a running projectile, the pressure probes would lead to a velocity aligning with that of the EM probe velocity. During an unstart, the velocity of the shock wave front was calculated by the data provided by pressure probes and the EM probes' data was used to calculate the velocity of the projectile.

4.3.1 EM Probe Response

As previously described, the EM probes are multiplexed such that all EM probes end up on six different channels into the DAS. Early on in the BTRA testing, it was noticed that there existed significant combustion noise relayed through these channels emanating from within the BT section. Therefore, EM probes were removed from the BT section for the rest of the testing. Figures 4.6 and 4.7 show results of a multiplexed channel of EM probes for three different shots; with EM probes in the baffled-tube section, and two different types of EM probes without any in the BT section. HS1923 (Figure 4.6) had an EM probe inside of the BT and significant noise can be seen making the entire signal worthless. For reference, green lines mark where pressure probes mark the projectile in time, no signal response on the EM channel can be distinguished. For clarity purposes, the time of the location designated by the pressure transducer is shown in Figure 4.6b, and shows no determinable EM response. The differences between HS1929 and HS1932 (Figure 4.7) are the types of EM probes used, however, neither shot had any EM probes in the BT section. HS1929 used the typical EM probes and got responses similar to that of past shots (on the order of $\sim$2-3 V) whereas HS1932 EM probes had significantly more copper winds (also known as "super mags") therefore increasing the magnitude of the response (on the order of $\sim$5-10 V). Both HS1929 and HS1932 show significant signal to noise ratio and the projectile location is visible and easily pinpointed. The shape of the EM signal response is very similar between the typical EM probe and the "super mags", but the amplitude is 2-3 times as great.

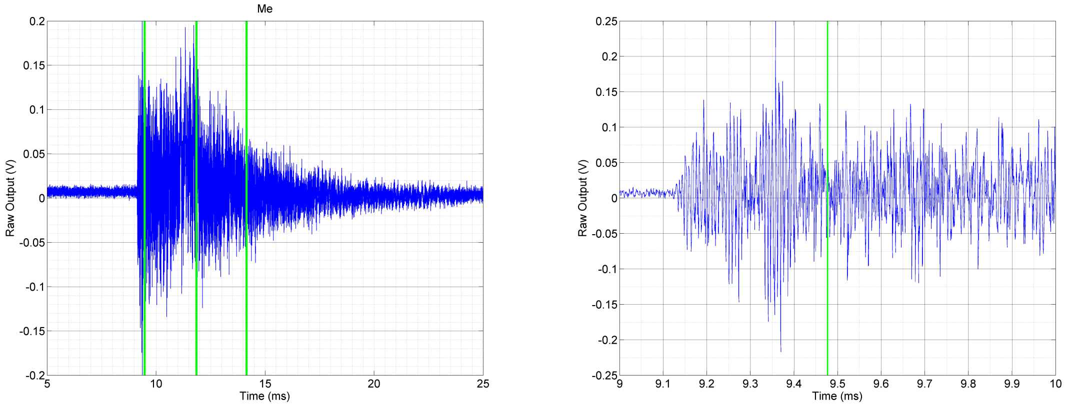

(a) HS1923 EM Channel E.

(b) HS1923 EM Channel E, focused around pressure signal.

Figure 4.6: HS1923 EM Channel E with projectile time overlay (from pressure transducer).

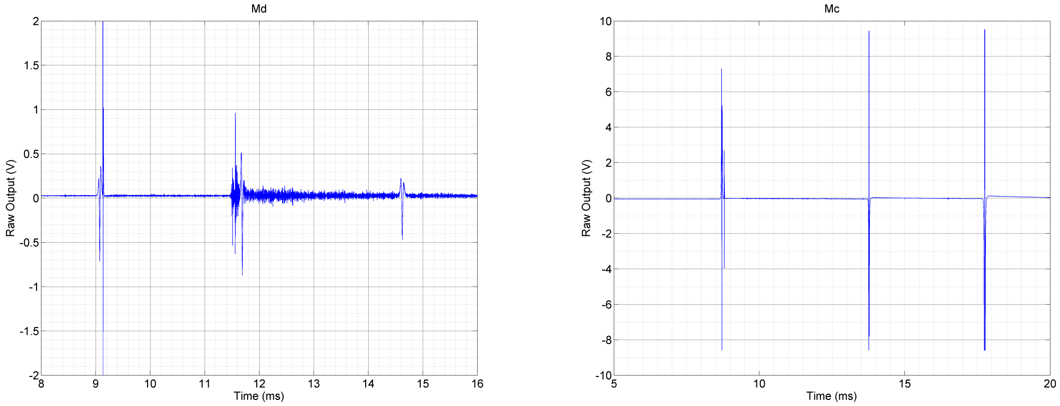

(a) HS1929 EM Channel D.

(b) HS1932 EM Channel C.

Figure 4.7: Comparison of different EM probe responses.

4.3.2 Pressure Transducer Response

The pressure transducers were used to examine the pressure field at the tube wall, provide data for wave velocities and as an alternate means for determining the projectile velocity.

Because the time-of-arrival of the leading pressure pulse is tracked, this allows the velocity of the unstart shock wave to be determined. While an unstart leads to no positive acceleration, it often makes a transition to a CJ wave; which can be helpful to verify the stoichiometric ratio of the propellants.

The following data were acquired from within the baffled-tube section from sensors centered between baffles showing a typical pressure signal for a running projectile. The stations shown are at the aft end of the BT and show approximately 80 meters per second increase in the 40-centimeters traveled. It is clear that many shock reflections are occurring within the chamber of the BT but a clear initial pressure rise, at 10.25 ms, and recovery before the pressure due to combustion, at 10.30 ms, is seen at station 6 (Figure 4.8a). This phenomenon is less visible at station 8 (Figure 4.8b), possibly due to the complex nature of the baffled-tube shock dynamics; regardless, an initial pressure drop is recorded and matches the projectile velocity as provided by EM probes outside the BT.

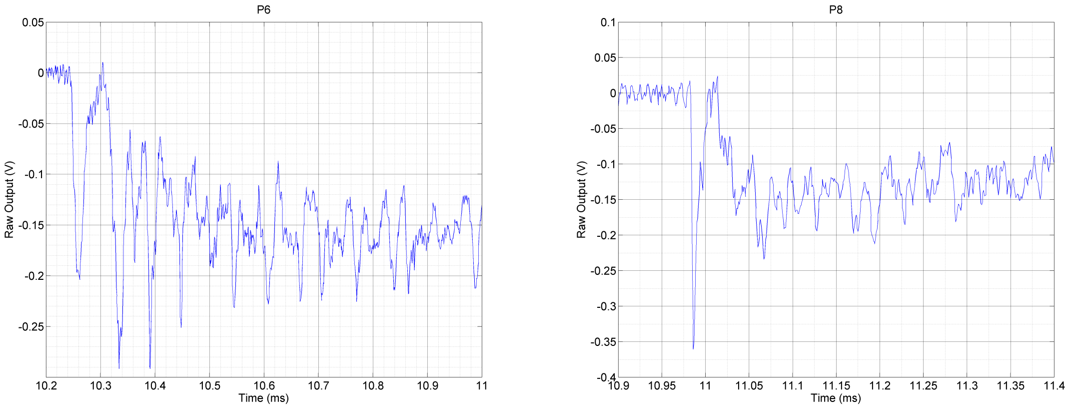

(a) HS1926 pressure trace at Station 6.

(b) HS1926 pressure trace at Station 8.

Figure 4.8: Pressure traces for running projectile - HS1926 in baffled-tube.

In attempts to test the upper non-dimensional heat release envelope of the BTRA, a $\Phi = 1.5$ methane-nitrous oxide mixture was tested which has a $Q \approx 16.1$ and a CJ detonation velocity of $V_{CJ} \approx 2395$ m/s. Both stations indicate an intense pressure rise with reflections after and no distinguishable projectile pressure which is representative of an unstart. A mean velocity of 2365 m/s (98.7% V_{CJ}) calculated between the stations shown in Figure 4.9 confirms an unstart as well as the experimental chemistry.

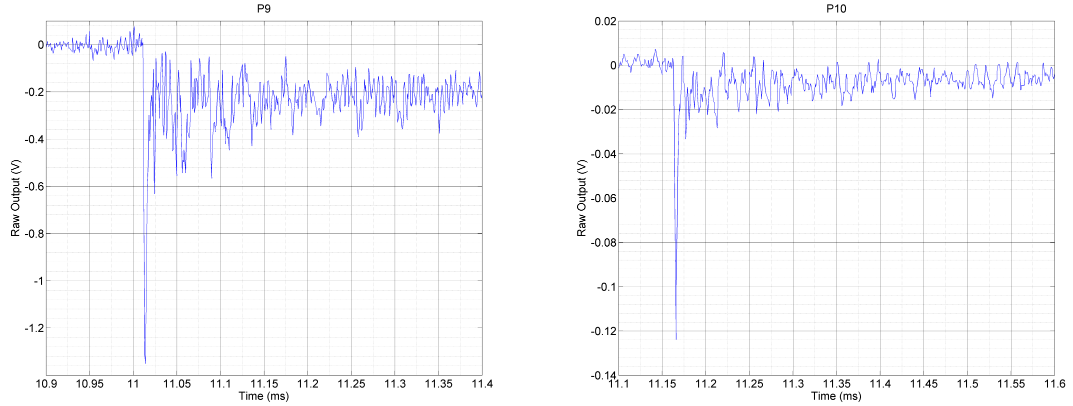

(a) HS1938 pressure trace at Station 9.

(b) HS1938 pressure trace at Station 10.

Figure 4.9: Pressure traces for unstarted projectile - HS1938 in baffled-tube.

In testing the low entrance speed capabilities of the BTRA, a $\Phi = 2$ methane-nitrous oxide mixture was tested which has a $Q \approx 13.9$. Data in Figure 4.10 are representative of a projectile followed by the combustion process moving at approximately 800 m/s (based on axial distance between instrument ports and time-of-arrival of the initial shock waves).

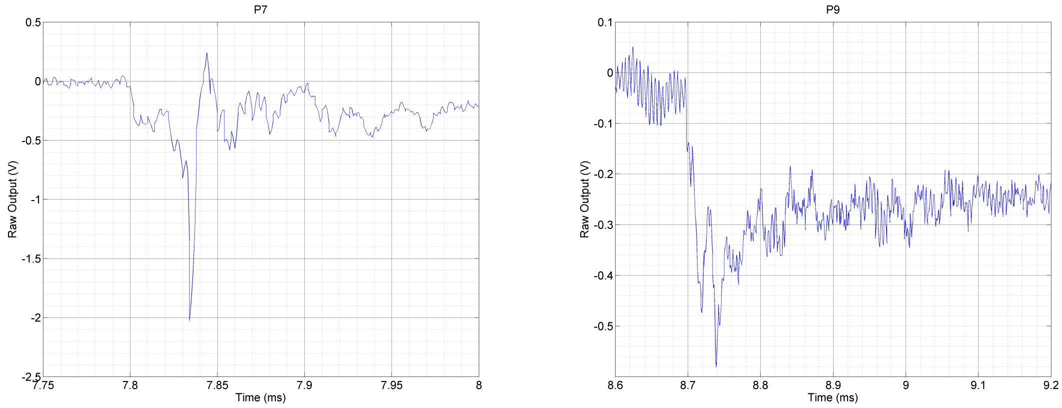

(a) HS1947 pressure trace at Station 7.

(b) HS1947 pressure trace at Station 9.

Figure 4.10: Pressure traces for running projectile - HS1947 in baffled-tube.

4.3.3 Velocity-Distance Plots for BTRA Testing

The BTRA testing proved to add a layer of difficulty in tracking of the projectile within the BT section as neither the EM probes or the pressure transducers were reliable due to various phenomena. As in the velocity deficit experiment, the mean velocity was calculated based upon the times at the stations directly upstream and downstream of the BT test section. An example of a typical hot shot is shown below in Figure 4.11 with indications for the start and end of the BT section. This particular shot shows approximately 100 meters per second gain in the 2-meter-long section and steep deceleration due to high pressure nitrogen (920 kPa) filling the sections downstream of the baffled-tube as a drag-brake mechanism.

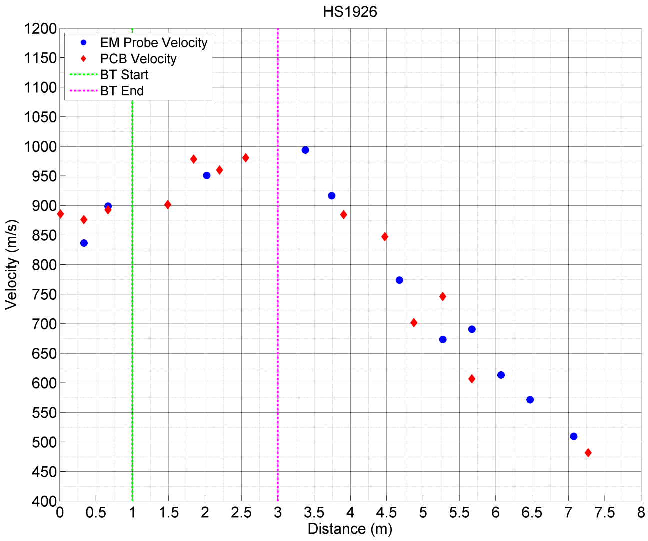

Figure 4.11: Velocity-distance plot for HS1926

4.3.4 Calculation of Experimental Thrust in BTRA Testing

The experimental thrust is calculated by assuming a constant acceleration in the BT. Therefore the following equation can be used to calculate the projectile's average acceleration ($\bar{a}$) based on the velocity going into and out of the BT section (u_i and u_f, respectively) and the change in distance ($\varDelta x$):

$$u_f^2 = u_i^2 + 2\bar{a}\varDelta x$$

$$\bar{a} = \frac{u_f^2 - u_i^2}{2\varDelta x} \tag{4.3}$$

Using the average acceleration and the mass of the projectile (m_p) the experimental force on the projectile is calculated:

$$F_{BT,exp} = m_p\bar{a}$$

In order to calculate the non-dimensional experimental thrust, the initial fill pressure and effective area are divided out.

$$I_{BT,exp} = \frac{F_{BT,exp}}{P_1 A_{eff}} = \frac{F_{BT,exp}}{P_1 A_b \beta}$$

Appendix E and Appendix F are the test logs and collection of all velocity-distance plots created during BTRA testing, respectively. The MATLAB code used to plot the velocity-distance diagrams of the baffled-tube experiments can be found in Appendix B.3.

Chapter 5

RESULTS AND DISCUSSION

“Science is not about making predictions or performing experiments. Science is about explaining.”

Bill Gaede

This chapter will collect the previous data sets and correlate the experiments into a new data set in order to show relations learned from the detonation testing that will be utilized in the theoretical performance model of the baffle-tube ram accelerator. The data produced for graphing the velocity deficit experiments can be found in Appendix D and the data produced for the baffled-tube ram shots can be found in Appendix F.

5.1 Velocity Deficit Experiment

A total of 28 detonation tests were performed through the baffled-tube with five failing to result in collected data (no trigger or never detonated). Initial testing was performed using a magneto connected directly to an automotive coil which proved to be unreliable and would not initiate a detonation every time. Once the ignition system was swapped for the ignition circuit designed by Professor Mattick, ignitions could reliably be performed up to an unknown pressure as the highest attempted was 450 kPa. Above this point, the hypothesized velocity deficit reduced to nil in each of the mixtures attempted. The plot in Figure 5.1 shows the trend of the average velocity deficit (measured both as an average of all ports, and a centered average) non-dimensionalized by the theoretical CJ detonation velocity versus initial fill pressure. Both measurements of velocity deficit indicate a similar trend, even if the numerical values are not exactly the same.

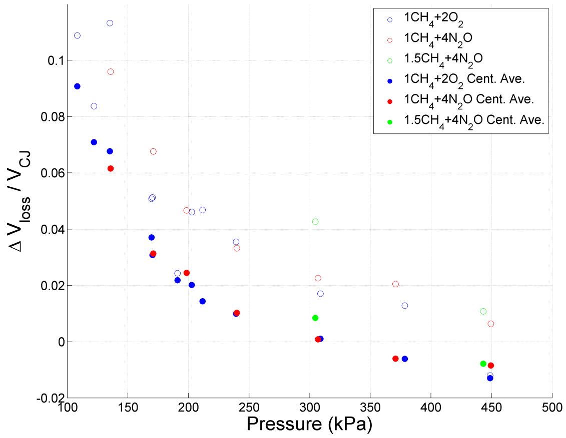

Figure 5.1: Velocity Deficit versus Fill Pressure

The results above match a similar trend in detonation cell size versus pressure produced by Manzhalei, Mitrofanov and Subbotin [26] are plotted below for stoichiometric methane-oxygen. It is hypothesized that the decreasing cell size, with increased fill pressure results in the detonation not being inhibited by the existence of the baffles. No such data set is known to exist for methane-nitrous oxide at the time of writing this thesis.

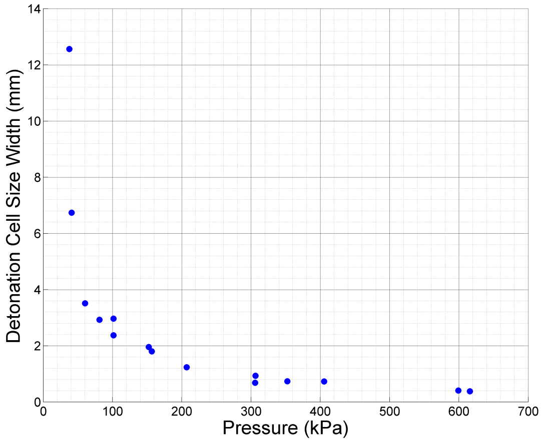

Figure 5.2: Experimental detonation cell size versus Fill Pressure ($1CH_4$+$2O_2$).

In the interest of including a way to approximate cell size from the velocity deficit, the following two-axis plot is included. The blue circles are the detonation cell size data for stoichiometric methane-oxygen and the black diamonds are the experimental velocity deficit, non-dimensionalized by the CJ detonation velocity. The detonation cell size at which the velocity deficit becomes null is approximately 1 millimeter. Gao, Ng and Lee [27] studied the minimum tube diameter for steady propagation of gaseous detonations in stoichiometric methane-oxygen and showed that the minimum diameter for propagation could be given by:

$$d_{min}\ [\text{mm}] = 161.88(P_0\ [\text{kPa}]^{-1.07}$$

at an initial fill pressure of 120 kPa (corresponding to where the deficit reduces to zero), this results in a minimum diameter of 1.06 millimeters, which is on the order of experimental error. The cell size (λ)can be approximated with data collected during their experimentation as well, by the following equation, and result in approximately 2.4 millimeters:

$$\lambda\ [\text{mm}] = 996.00(P_0\ [\text{kPa}]^{-1.28}$$

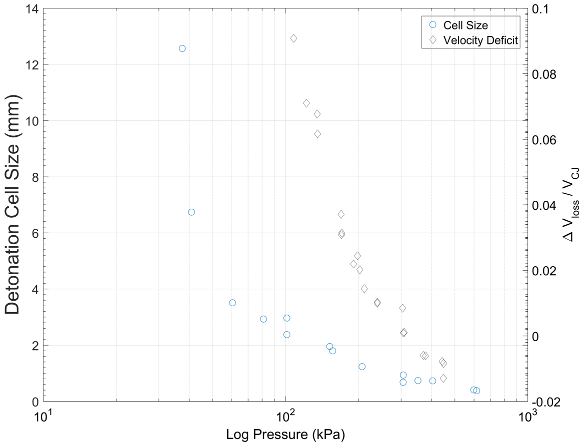

Figure 5.3: Experimental detonation cell size ($1CH_4$+$2O_2$) and velocity deficit versus fill pressure (Log scale).

Based on the interpreted results of the detonation velocity experiments, no detonations were attempted above 450 kPa, and the data acquired was not used as an experimental method to validate the CJ Mach number of propellants in the BTRA which do show a deficit of the CJ Mach number in experiments.

5.2 Baffle-Tube Ram Shots

A total of 27 baffled-tube ram accelerator experiments were performed with two failing to result in collected data (no trigger) and one with extraneous noise making the signal not meaningfully discernible. Of the remaining 24 experiments, 17 resulted in positive acceleration; the other half had issues such as not meeting a minimum entrance Mach number, propellants with too high of Q, or human error in the shot process.

The following table shows the initial and final velocities, projectile mass and calculated non-dimensional experimental thrust of each of the positively ram accelerated experiments (only these experiments will be considered from this point forward). Also provided is the experiment's average Mach number ($\bar{M}$) corresponding to the average velocity.

Table 5.1: BTRA Experimental Results

Shot Name	u_i (m/s)	u_f (m/s)	m_p (g)	P_1 (MPa)	$\bar{M}$	$I_{BT,exp}$	Chemistry
HS1923	919	1020	139.8	1.02	3.29	1.92	$1CH_4 + 2O_2 + 5CO_2$
HS1926	900	1050	145.6	1.02	3.12	3.03	$1CH_4 + 2O_2 + 2CO_2$
HS1927	910	950	148.8	0.997	3.01	0.81	$1CH_4 + 2O_2 + 2.4CO_2$
HS1929	854	975	149.1	1.02	2.92	2.36	$1CH_4 + 2O_2 + 2CO_2$
HS1930	856	900	127.6	1.02	2.80	0.70	$1CH_4 + 2O_2 + 1.9CO_2$
HS1931	815	987	128.5	1.22	2.88	2.36	$1CH_4 + 2O_2 + 2CO_2$
HS1932	797	970	145.7	1.23	2.81	2.64	$1CH_4 + 2O_2 + 1.9CO_2$
HS1933	748	927	143.7	1.00	2.66	3.12	$1CH_4 + 2O_2 + 1.9CO_2$
HS1936	793	944	145.6	1.22	2.76	2.27	$1CH_4 + 2O_2 + 1.9CO_2$
HS1937	842	971	145.8	1.01	3.00	2.45	$2CH_4 + 4N_2O$
HS1939	844	1010	145.7	1.54	3.07	2.17	$2CH_4 + 4N_2O$
HS1941	845	1080	139.4	1.53	3.17	2.94	$2CH_4 + 4N_2O$
HS1942	1050	1150	139.8	1.02	3.62	2.34	$2CH_4 + 4N_2O$
HS1943	844	1070	140.2	2.13	3.15	2.04	$2CH_4 + 4N_2O$
HS1944	1110	1220	139.5	1.54	3.85	1.80	$2CH_4 + 4N_2O$
HS1945	732	935	139.9	1.02	2.75	3.39	$2CH_4 + 4N_2O$
HS1947	613	875	138.7	1.54	2.46	2.57	$2CH_4 + 4N_2O$

The BTRA test series was comprised of two classes of mixtures, methane-oxygen-carbon dioxide and methane-nitrous oxide. The range of operational ram acceleration Mach numbers was from 2.02 to 4.04, which were both in the methane-nitrous oxide propellant. Prior to these tests, the lowest entrance velocity recorded with positive ram acceleration was 700 meters per second [28], the tests performed with the BTRA yielded a minimum entrance of 610 meters per second (see velocity-distance plot in Figure 5.4) which is a 13% reduction.

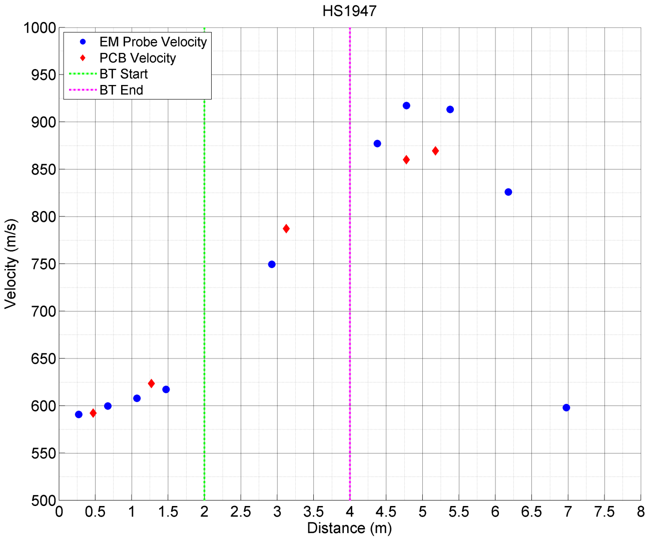

Figure 5.4: Velocity-distance plot for HS1947

The following results take into account the potential chemical energy equalization with the void volume ratio, β. The theoretical curves are based on the TCRA code developed by Depraz [10] and are compared to an equivalent baffled-tube system by dividing the non-dimensional thrust by β as per Equation 2.7 to achieve $I_{SBRA,eff}$. The theoretical curves for the two mixtures are compared with the corresponding experimental non-dimensional thrust data found in Table 5.1 plotted at the average Mach number during the experiment in the BT section are shown in Figure 5.5. Both classes of propellants show significant deviation from the theoretical values of non-dimensional thrust. More significant is that below the maximum-thrust-Mach number, the non-dimensional thrust should be greater than theory according to the drag model offered. The possible cause for this deviation will be discussed later in Section 5.3.

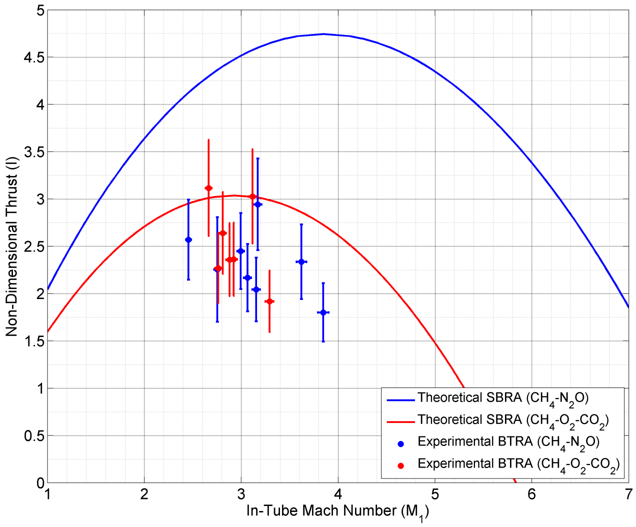

Figure 5.5: Experimental BT Non-Dimensional Thrust compared to Theoretical Curves.

In order to better categorize the deficit in non-dimensional thrust indicated, the deficit is plotted as a ratio to the theoretical non-dimensional thrust expected. The non-dimensional deficit is calculated according to the following equation:

$$I_{deficit} = I_{SBRA,eff} - I_{BT,exp}$$

Figure 5.6 indicates a large variation of the deficit in terms of Mach number; however, the methane-nitrous oxide mixture shows a relatively consistent deficit of 50% of the theoretical equivalent non-dimensional thrust. The methane-oxygen-carbon dioxide mixture shows a much wider range of results from 0 to 80% of thrust deficit. The two outlying points at 75 to 80% seem to be anomalies based on the other 7 experiments in the same mixture with very little deviation in experimental setup. Therefore these can be considered outliers to the data set; ergo, the methane-oxygen-carbon dioxide class mixture indicates a non-dimensional deficit of approximately 15% of the theoretical equivalent non-dimensional thrust of a SBRA.

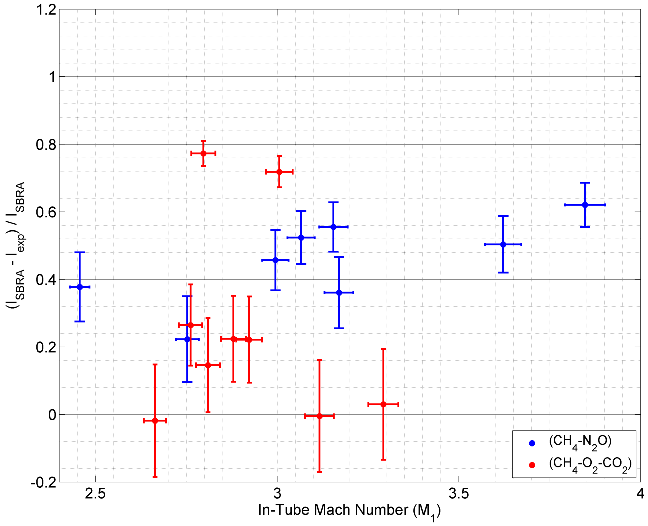

Figure 5.6: Experimental BT Non-Dimensional Thrust Deficit as percentage of Theoretical Thrust.

In comparing the performance benefits of what the addition of baffles to an existing smooth-bore system might be, the dimensional thrust per unit fill pressure was considered for the experimental data set, and also the theoretical equivalent system. Figure 5.7 indicates that for a given SBRA, when baffles are inserted, and high Q mixtures are used that performance increases of 30 to 100% can be expected.

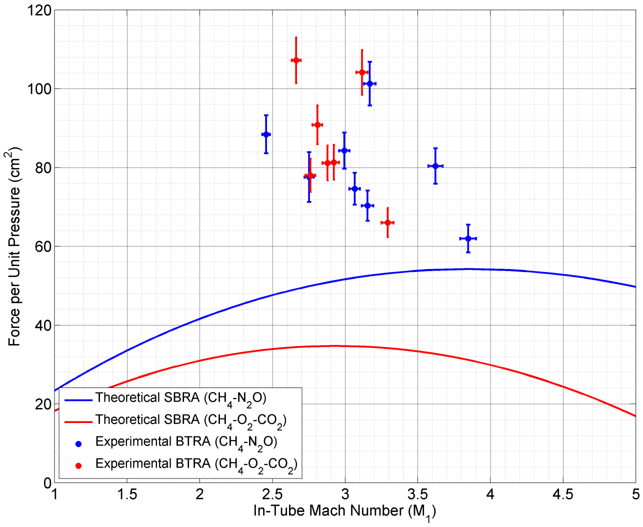

Figure 5.7: Experimental BT Thrust per unit fill pressure compared to Theoretical Curves.

5.2.1 Combustion Indicators on Baffled-Tube Inserts

During inspection of the baffled-tube inserts after ram accelerator shots were performed, macroscopic patterns appeared on the rail sections of each pocket in approximately the same location in each baffle. No work has been performed on accounting for the size, location or reasoning; however, the existence of these patterns seemed like an important addition in completeness of describing the experimental results. The markings can be seen in Figure 5.8.

Figure 5.8: Combustion pattern on the baffled-tube inserts' rails.

5.3 Combustion Sensitivity Study

Even before including the revised drag model into the thrust equation, the experimental non-dimensional thrust data did not correlate with the main benefit of the addition of the baffles. In reevaluating the reactive CFD results, noticeable reactants remain in the baffle chambers during the combustion process resulting in a non-perfect combustion efficiency. [16] In order to best account for this imperfection, a combustion efficiency parameter, η_Q, is multiplied by the non-dimensional heat release, Q. Making the equation for non-dimensional thrust:

$$\frac{F}{P_1 A_b} = M_1 \frac{\gamma_1}{\gamma_2}(1+\gamma_2)\sqrt{\left(\frac{\gamma_2 - 1}{\gamma_1 - 1}\right)\left(\frac{\eta_Q Q + \frac{h_1}{c_{p1} T_1} + \frac{\gamma_1 - 1}{2} M_1^2 - \frac{D(\gamma_1 - 1)}{P_1 A_b \gamma_1}}{\frac{h_2}{c_{p2} T_2} + \frac{\gamma_2 - 1}{2}}\right)} - (1+\gamma_1 M_1^2) - \frac{D}{P_1 A_b} \tag{5.1}$$

In performing a sensitivity study of the variation of η_Q, the state 2 variables will be assumed to remain constant, as if complete combustion occurred. Including incomplete combustion due to the baffles, is not a capability of the modified CEA code in the current state. For this study only the methane-nitrous oxide class propellant will be considered for simplicity. Figure 5.9 indicates the results for variations of η_Q from unity (complete combustion) to 0.4 for the methane-nitrous oxide mixture. These variations cause the CJ detonation Mach number, the maximum-thrust, and corresponding maximum-thrust Mach number to decrease significantly.

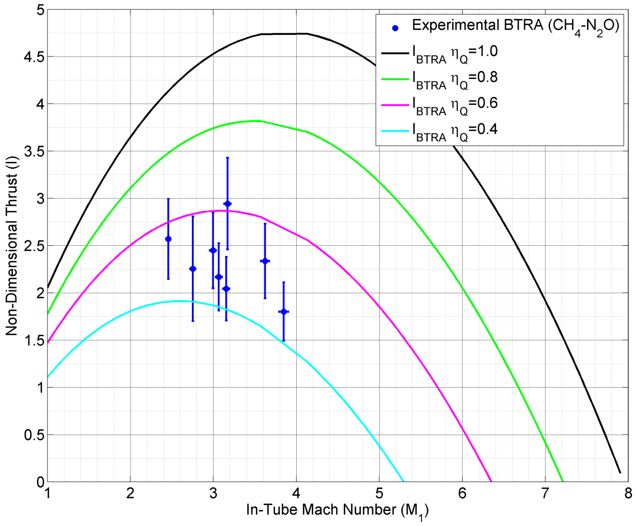

Figure 5.9: Non-dimensional thrust, without drag, varying η_Q parameter.

If the revised drag model would be applied to the approximation of the incomplete combustion by varying η_Q, the zero drag point would remain local to the $\eta_Q = 1.0$ corresponding Mach number. The nature of the issue is that the state 2 variables are dependent on the heat release. In order to conserve the state 2 variables corresponding to complete combustion, the system could be modeled with a greater void volume, thus increasing the β term, and make the system comparable to an incomplete combustion phenomenon. In order to look at how variations of this term effect the non-dimensional thrust compared to experimental data, a void volume ratio parameter is introduced, η_β, as follows:

$$I_{BTRA} = \frac{I_{SBRA}}{P_1 A_b \beta \eta_\beta} \tag{5.2}$$

In using the η_β parameter, the CJ detonation Mach number and Mach number corresponding to the maximum thrust point are conserved; however, the maximum thrust is dropped by a factor of η_β. Figure 5.10 indicates a decreasing maximum thrust point for each value of η_β, while maintaining the boundary conditions.

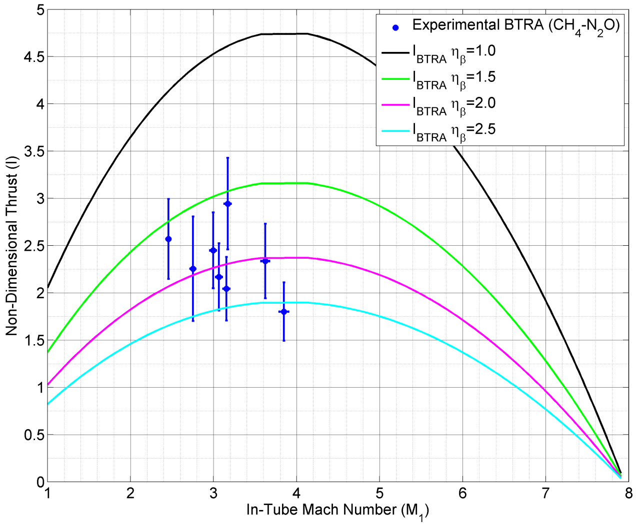

Figure 5.10: Non-dimensional thrust, without drag, varying η_β parameter.

By choosing a value of η_β value that is centralized in the experimental data, the drag model can be used and conservation of the zero drag condition at the maximum thrust point will remain consistent. $\eta_\beta > 1.0$ corresponds to a larger effective area; one can think of the complete combustion of the propellants in the actual system occurring in a BT with deeper chambers resulting in incomplete combustion. Figure 5.11 uses a value of $\eta_\beta = 2.0$ and varies the drag parameter, c_d, from 0.015 to 0.15 to show what an order of magnitude change looks like in the modeling of drag in the baffled-tube. No promising value of the drag parameter is clear but it seems that in attempting to model the incomplete combustion phenomenon, the deficit in experimental non-dimensional thrust has decreased; presumably a better model of the baffled-tube ram accelerator.

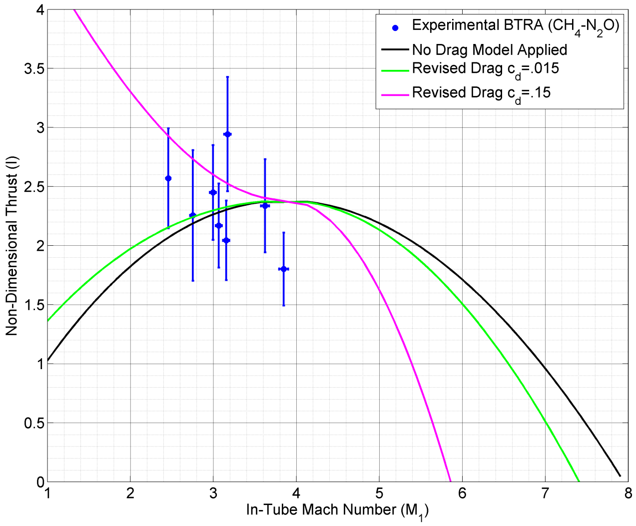

Figure 5.11: Non-dimensional thrust, with $\eta_\beta = 2.0$ and varying drag parameter, c_d.

Chapter 6

CONCLUSIONS AND FUTURE STUDY

"It is one thing to be clever and another to be wise."

George R. R. Martin

6.1 Conclusions

A performance model and drag model are offered for the baffled-tube ram accelerator to be compared with a traditional smooth-bore ram accelerator system. Both models are meant to simplify the extremely complex flow and combustion field around the baffles. In order to quantify how well these simplifications are, two main experiments were performed: the velocity deficit measurement of a detonation wave through the baffle-tube and ram accelerator shots.

While attempting to measure a velocity deficit of a detonation through the baffled-tube at varying fill pressure, three classes of mixtures were considered (stoichiometric CH_4-O_2 and CH_4-N_2O and CH_4-N_2O at $\Phi = 1.5$). All tests showed a decrease of velocity deficit when the fill pressure was increased, to the point of zero deficit at pressures of approximately 450 kPa; this trend is associated with the reduction of detonation cell size width at increasing pressure.

In exploring the operational envelope of the baffled-tube ram accelerator, two main classes of propellants (CH_4-O_2-CO_2 and CH_4-N_2O) were tested with axisymmetric projectiles. With experimental results showing 15 to 50% non-dimensional thrust deficits, the current performance and drag model has much room for refinement but the further modeling of incomplete combustion seems promising. Both classes of mixtures showed promising results when compared on a thrust per unit fill pressure basis with 30 to 100% increase over the corresponding theoretical values for a smooth-bore ram accelerator.

All in all, the baffled-tube ram accelerator with non-optimally designed inserts works! Ram accelerator shots were performed with propellant non-dimensional heat release of 12-13, doubling the previous maximum values performed in the smooth-bore system. Further, the minimum velocity to successfully accelerate was reduced from 700 meters per second to 610 meters per second.

6.2 Future Study

As this is the preliminary experimentation performed on the baffled-tube ram accelerator, the future is extremely rich in promising research. The envelope of operation has yet to be explored outside of a small portion of the Mach number capabilities of the baffled-tube ram accelerator - especially the high Mach number regime to solidify comparison points for the drag model.

Once more mixtures and more of the operational envelope has been experimented in, the drag and performance models will be able to be refined. The modeling of the incomplete combustion seems to be the largest factor in the non-dimensional thrust deficit when compared to theory which also leads to question initial assumptions of a choked-plane in the baffled-tube. Comparison between smooth-bore and baffled-tube luminosity measurements of combustion may also be able to determine a level of incompleteness of the combustion process. The same experiment could be used to compare with CFD results for the number of chambers behind the projectile effected by combustion.

The application of using the baffled-tube as an initial stage for finned projectiles has yet to be explored, but has significant potential in reducing the minimum entrance velocity requirements on a pre-launcher system for projectiles of increased mass.

BIBLIOGRAPHY

[1] Knowlen, C., and Bruckner, A. P., **Direct Space Launch Using Ram Accelerator Technology**, *Space Technology and Applications International Forum*. American Institute of Physics. 2001.

[2] Knowlen, C., Joseph, B., and Bruckner, A. P., **Ram Accelerator as an Impulsive Space Launcher: Assessment of Technical Risks**, *International Space Development Conference*. Dallas, TX, May 25-28, 2007.

[3] Hertzberg, A., Bruckner, A. P., and Bogdanoff, D. W., **Ram Accelerator: A New Chemical Method for Accelerating Projectiles to Ultrahigh Velocities**, *AIAA Journal*, Vol. 26, No. 2, 1988, pp. 195-203.

[4] Bruckner, A. P., Knowlen, C., Hertzberg, A., and Bogdanoff, D. W., **Operational Characteristics of the Thermally Choked Ram Accelerator**, *J. of Propulsion and Power*, Vol. 7, No. 5, 1991, pp. 828-836.

[5] Higgins, A. J., Knowlen, C., and Bruckner, A. P., **Ram Accelerator Operating Limits, Part 1: Identification of Limits**, *J. of Propulsion and Power*, Vol. 14, No. 6, 1998, pp. 951-958.

[6] Higgins, A. J., Knowlen, C., and Bruckner, A. P., **Ram Accelerator Operating Limits, Part 2: Nature of Observed Limits**, *J. of Propulsion and Power*, Vol. 14, No. 6, 1998, pp. 959-966.

[7] Kruczynski, D., **Experimental Demonstration of a 120 mm Ram Accelerator**, *29th JANNAF Combustion Subcommittee Meeting*, NASA Langley Research Center, Hampton, VA, Oct. 19-23,1992.

[8] Giraud, M., Legendre, J. F., and Simon, G., **Ram Accelerator Studies in 90 mm Caliber**, *43rd Meeting of the Aeroballistic Range Association*, Columbus, OH, Sept. 28-Oct. 2, 1992.

[9] Wieland Naumann, K., and Bruckner A. P., **Ram Accelerator Ballistic Range Concept for Softly Accelerating Hypersonic Free-Flying Models**, *J. of Aircraft*, Vol. 31, No. 6, 1994.

[10] Depraz, S., **New Tools for Ram Accelerator Performance Modeling**, *MSAA Thesis*, University of Washington, July, 2007.

[11] Knowlen, C., **Theoretical and Experimental Investigation of the Thermodynamics of the Thermally Choked Ram Accelerator**, *Ph.D. Dissertation*, University of Washington, April, 1991.

[12] Knowlen, C. and Bruckner, A.P., **A Hugoniot Analysis of the Ram Accelerator**, *Shock Waves*, Vol I, Proceedings of the 18th Intl Symposium on Shock Waves, Sendai, Japan, Takayama, K., ed., Springer-Verlag, Berlin, pp. 617-622, 1992.

[13] Higgins, A. J., Knowlen, C., and Kiyanda, C. B., **Gasdynamic Operation of Baffled Tube Ram Accelerator in Highly Energetic Mixtures**, *20th International Colloquium on the Dynamics of Explosions and Reactive Systems*. McGill University, Montreal, Canada, July 31 August 5, 2005.

[14] Higgins, A. J., **Ram Accelerators: Outstanding Issues and New Directions**, *J. of Propulsion and Power*, Vol. 22, No. 6, 2006, pp. 1170-1187.

[15] Gu, L. S., Knystautas, R., and Lee, J. H., **Influence of Obstacle Spacing on the Propagation of Quasidetonation**, *Progress in Aeronautics and Astronautics*, Vol. 114, 1988, pp. 232-247.

[16] Daneshvaran, N. and Knowlen C., **Transient computational fluid dynamic modeling of baffled-tube ram accelerator**, Accepted for presentation at *55th AIAA Aerospace Sciences Meeting*. Gaylord, TX, Jan. 9-13, 2017.

[17] Tanguay, V., and Higgins, A., **On the Inclusion of Frictional Work in Non-Ideal Detonations**, *20th International Colloquium on the Dynamics of Explosions and Reactive Systems*. McGill University, Montreal, Canada, July 31August 5, 2005.

[18] Bengherbia, T., Yao, Y., Bauer, P., Knowlen, C., Bruckner, A. P., and Giraud, M., **One-Dimensional Modeling of Thermally Choked Ram Accelerator Based on CFD Simulations**. *50th AIAA Aerospace Sciences Meeting*. Nashville, TN, Jan. 9-12, 2012.

[19] Bauer, P., Knowlen, C., Bruckner, A. P., Henner, M., Legendre, J. F., and Giraud, M., **Determination of the choke pressure of a ram accelerator projectile in subdetonative regime**. *J. Phys.*, Vol. 4, No. 10, 2000, pp. 59-67.

[20] Bundy, C., Knowlen, C., and Bruckner, A. P., **Unsteady Effects on Ram Accelerator Operation at Elevated Fill Pressures**, *J. of Propulsion and Power*, Vol. 20, No. 5, 2004, pp. 801-810.

[21] Knowlen, C., Bundy, C., Schwab, R., and Bruckner, A. P., **University of Washington High Pressure Ram Accelerator Facility**, *Proceedings of the 50th Aeroballistic Range Association*, Pleasanton, CA, November 8-12, 1999.

[22] Bogdanoff, D. W., Knowlen, C., Murakami, D., and Stonich, I., **Magnetic Detector for Projectiles in Tubes**, *AIAA Journal*, Vol. 28, No. 11, 1990, pp. 1942-1944.

[23] Heflin, L. **Baffled-Tube Ram Accelerator Structural Design**, *AIAA Region VI Student Conference*, Corvallis, OR, April 1-3, 2016.

[24] Daneshvaren, N., **Transient computational fluid dynamic modeling of baffled tube ram accelerator in Eulerian frame of reference**, *AIAA Region VI Student Conference*. Corvallis, OR, April 1-3, 2016.

[25] Christofferson, E. C., **A Magnetic Transducer Detection System for High Speed Projectiles in Tubes**, *MSAA Thesis*, University of Washington, 1989.

[26] Manzhalei, V. I., Mitrofanov, V. V. and Subbotin, V. A., **Measurement of inhomogeneities of a detonation front in gas mixtures at elevated pressures**. *Combustion Explosion Shock Waves (USSR)*, Vol. 10, 1974, pp. 89-95.

[27] Gao, Y., Ng, N. and Lee, J. H. S., **Minimum tube diameters for steady propagation of gaseous detonations**. *Shock Waves*, Vol. 24, Iss. 4, July 2014, pp. 447-454.

[28] Knowlen, C., Schultz, E., and Bruckner, A. P., **Investigation of Low Velocity Starting Techniques for the Ram Accelerator**, *33rd AIAA/ASME/SAE/ASEE Joint Propulsion Conference and Exhibit*, Seattle, WA, July 6-9, 1997.

Appendix A

SPARK BOX SCHEMATIC

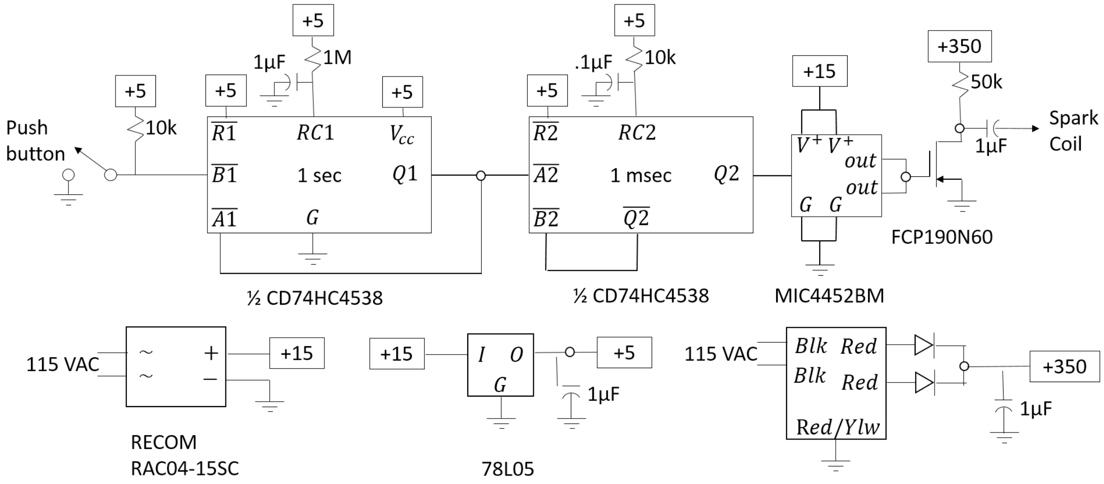

Figure A.1: Spark ignition circuit diagram with part call-outs.

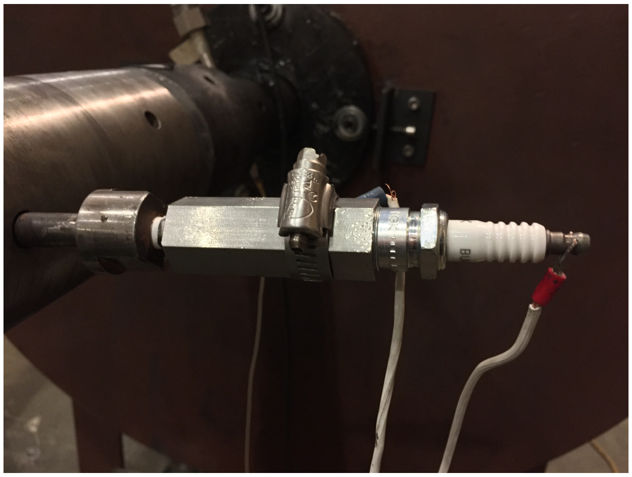

Figure A.2: Spark plug installation photograph.

Appendix B

BAFFLE-TUBE RAM SHOT AND DETONATION SHOT POST-PROCESSING

B.1 Raw Data Batch Plot

```
clear all;close all;clc
%Change filename to the shot folder
filename = 'CS79';
%Change test section station numbers for final pressure plot
test_section=6:10;
calibration=0;
disp('JG 8/12/16');
%% Data procurement from LABview output file and Instrumentation Log
%creates color scheme of most diverse colors
colors=distinguishable_colors(10);
colors(4,:)=[]; colors(6,:)=[];
%moves directory into the folder of the shot name
cd(filename);
fid = fopen(filename);
A = textscan(fid,'%f','headerlines',23);
num_samples = length(A{1})/33;
%creates matrix of data
big_data = reshape(A{1},33,num_samples)';
sample_rate = num_samples/big_data(end,1);
%creates matrix of data
big_data = reshape(A{1},33,num_samples)';
%this file must exist within the shot file
loadstring=['Instrument Log_' filename '.xlsx'];
%DAS Modules setup
[num,textin]=xlsread(loadstring,'I21:P24');
%MAG Strings
[magnum,magtext]=xlsread(loadstring,'H4:P9');
%Calibration data
[pcalnum,pcalname]=xlsread(loadstring,'S5:T50');
%Probe positions
[i_pcalnum,i_pcalname]=xlsread(loadstring,'F3:F46');
fclose(fid);
cd ..
%% Creation of arrays and indexing of Mag and Pressures
i_pcalname(1)=[]; %getting rid of 'Cable' from beginning of string and
```

```
%to guarantee no dropped values
pnums=1:42; %all possible stations
for j=1:length(pnums)
pressure{j}=['P' num2str(pnums(j))]; %adding P in front as to match
%instrumentation log
end
pressure=['PLt' pressure]'; %adding in PLt to possible pressure locations
magnet={'Ma' 'Mb' 'Mc' 'Md' 'Me' 'Mf'}; %create all mag string
%possibilities
for j=1:length(i_pcalname)
    %array of calibrated probles next to all possible P locations
    pressure{j,2}=i_pcalname{j};
end
for j=1:length(magnet)
    %Finds the matrix locations of where magstrings are located in the DAS
    index_mag(j)=find(strcmp(magnet{j},textin));
end
jj=0;
mask=[0:7;8:15;16:23;24:31]; %match DAS input numbers (entered to get data)
for j=1:length(pressure)
    %find which pressure locations are being used and where to create an
    %array of used values (index_pressure) and their calibration data
    index_check=find(strcmp(pressure{j,1},textin));
    if ~isempty(index_check)
        jj=jj+1;
        index_pressure(jj,1)=find(strcmp(pressure{j,1},textin));
        plot_pressure{jj}=pressure{j};
%         pressure{jj,3}=.09;
        if ~isempty(pressure{j,2})
            index_cal=find(strcmp(pressure{j,2},pcalname));
            pressure{j,3}=pcalnum(index_cal);
        else
            pressure{j,3}=.09;
        end
        pressure{j,4}=index_pressure(jj);
        pressure{j,5}=mask(pressure{j,4});
    end
end
%index_pressure(index_pressure(:,2)==0,2)=.09; %Nominal value if no
%calibration data mask=[0:7;8:15;16:23;24:31]; %match DAS input numbers
%(entered to get data)
masked_mag=mask(index_mag); %mag inputs for DAS
for j=1:length(pressure)
    if ~isempty(pressure{j,5})
        if calibration==1
         big_data(:,pressure{j,5})=big_data(:,pressure{j,5})/pressure{j,3};
        end
    end
end
masked_pressure=[pressure{:,5}];
```

```
%masked_pressure;
big_data(:,1)=1000*big_data(:,1); % converting seconds to milliseconds
%% Plotting of Mag and Pressure data for all given stations
for j=length(masked_pressure):-1:1
    f=figure;
    for jj=1:length(masked_mag)
        %Plot Mag data normalized by the absolute maximum voltage
        plot(big_data(:,1),big_data(:,masked_mag(jj)+2)/...
            max(abs(big_data(:,masked_mag(jj)+2))),'Color',colors(jj,:));
        hold on
    end
    %Plot calibrated pressure data
    plot(big_data(:,1),big_data(:,masked_pressure(j)+2),'Color',...
        colors(jj+2,:),'LineWidth',1.2);
    hold off
    title(plot_pressure{j})
    %Changes name of plot in the windows system
    set(f,'name',plot_pressure{j},'numbertitle','off')
    xlabel('Time (ms)')
    if calibration==1
        ylabel('Pressure (psi) | Normalized Mag Response')
    else
        ylabel('Uncalibrated Pressure | Normalized Mag Response')
    end
    legend('Ma','Mb','Mc','Md','Me','Mf','Pressure Data','Location'...
        ,'SouthEast');
end
%% Holds the plots while user inputs data into New BT Data
input=menu('Click data saved button when finished inputting data into NEW BT DATA, Exit
    'Data Saved - Plot Pressure with Mags','Exit Program',...
    'Plot Individual Data Inputs');
switch input
    case 1
    case 2
        disp('Code has been terminated by user.')
        break
    case 3
        close all
        plots= [masked_mag,masked_pressure];
        titles= [magnet,plot_pressure];
        for j=length(plots):-1:1
            port_num=plots(j);
            f=figure;
            plot(big_data(:,1),big_data(:,port_num+2))
            title(titles{j})
            set(f,'name',titles{j},'numbertitle','off')
        end
        input=menu('Click Data Saved when finished inputting data into NEW BT DATA.',...
            'Data Saved - Plot Pressure with Mags','Exit Program');
        switch input
```

```
            case 1
            case 2
                disp('Code has been terminated by user.')
                break
        end
end
%% Creates Pressure plots with mag references based on New BT Data inputs
close all
loadstring='New BT Data.xlsx';
%Only saves the first mag and pressure time
[num2,magnames]=xlsread(loadstring,filename,'C29:I72');
num2(isnan(num2))=0; %turns blanks into zeros
num2(:,[1,2,3,5,6])=[]; %gets rid of mag-2 pres b4correction
%num2=num2*.001; %converts to seconds
num2(end,:)=[];
magnames(:,[1,3:end])=[];
pnum2=find(num2(:,2)~=0);%finds places pressure data is recorded
pnum2=pnum2-1;
for j=1:length(pnum2)
    pressure2{j}=['P' num2str(pnum2(j))]; %Creates pressure station names
    if find(strcmp(pressure2{j},'P0'))== 1;
        pressure2{j}='PLt'; %if P0 exists, it is PLt
    end
end
pressure2=pressure2';
for j=1:length(pressure2)
    ind_p(j,1)=find(strcmp(pressure2{j},pressure));
end
clear pressure2
pressure2{j,:}=pressure(ind_p,:);
pressure2=pressure2{1,1};
num2=num2(pnum2+1,:);
pindex=floor(num2(:,2)*sample_rate/1000);
deltime=floor(200e-6*sample_rate);
if exist([filename '/Images'],'dir') ~= 7
    mkdir([filename '/Images']);
end
index_pressure2=[pressure2{:,5}];
for j=1:length(index_pressure2)
    f=figure;
    set(f,'name',pressure2{j,1},'numbertitle','off')
    indices=pindex(j)-deltime:pindex(j)+4*deltime;
    %if num2(j,1)*sample_rate < pindex(j)+4*deltime
        plot(big_data(indices,1),big_data(indices,pressure2{j,5}+2))
        minp=min(big_data(indices,pressure2{j,5}+2));
        maxp=max(big_data(indices,pressure2{j,5}+2));
    title(pressure2{j,1})
    if num2(j,1)==0
        title([pressure2{j,1} ' - No Mag at Station'])
    else
```

```
        hold on
        plot([num2(j,1),num2(j,1)],[minp,maxp],'m')
        title(pressure2(j,1))
    end
    xlabel('Time (ms)')
    if calibration==1
        ylabel('Calibrated Pressure (psi)')
    else
        ylabel('Uncalibrated Pressure')
    end
    cd(filename)
    cd('Images')
    saveas(gcf,[filename '_' pressure2{j,1}],'png');
    cd ..
    cd ..
end
for j=1:length(test_section)
    pressure3{j}=['P' num2str(test_section(j))];
    %Creates pressure station names
end
for j=1:length(pressure3)
    ind_p2(j,1)=find(strcmp(pressure3{j},pressure));
end
clear pressure3
pressure3{j,:}=pressure(ind_p2,:);
pressure3=pressure3{1,1};
test_section_pnum=pnum2( pnum2>= test_section(1)...
    & pnum2 <= test_section(end));
indices = 11251:15001;
%indices=8751:12511;
f=figure;
set(f,'name','Pressure Plot','numbertitle','off')
for j=1:length(test_section_pnum)
   plot(big_data(indices,1),test_section_pnum(j)+big_data...
       (indices,pressure3{test_section_pnum(j)-5,5}+2),'Color',colors(j,:))
   hold on
end
xlabel('Time (ms)','FontSize',18); ylabel('Station Number','FontSize',18)
title([filename ' Test Section Pressure Plots'],'FontSize',18)
grid on
cd(filename)
cd('Images')
saveas(gcf,[filename '_Pressures'],'png');
cd ..
cd ..
cd 'Pressure Plots'
saveas(gcf,[filename '_Pressures'],'png');
cd ..
display('4 8 15 16 36 42')
display('Done')
```

B.2 BTD Batch Plot

```
clear all; close all;clc;set(0,'DefaultAxesFontSize',16)
%all BTD shots performed
filename = {'BTD02','BTD03','BTD06','BTD07','BTD08','BTD10','BTD11',...
    'BTD12','BTD13','BTD14','BTD15','BTD16','BTD18','BTD19','BTD20',...
    'BTD21','BTD22','BTD23','BTD24','BTD25','BTD27','BTD28'};
%initializing zero vectors
vcj=zeros(1,length(filename)); psig=zeros(1,length(filename));
btavev=zeros(1,length(filename)); defave=zeros(1,length(filename));
aves=zeros(2,length(filename));
for i=1:length(filename)
loadstring='New BT Data.xlsx';
[num,textin]=xlsread(loadstring,filename{i},'Z30:AA60');
aves(:,i)=num(end,:); num(end,:)=[];
xlab=num(:,1);
xlab(isnan(xlab))=[];
vwav=num(:,2);
vwav(isnan(vwav))=[];
bt=[2,4];
btstart = [2,2];
btend = [4,4];
vcj(i)=xlsread(loadstring,filename{i},'Z25');
vcjvec =[vcj(i) vcj(i)];
psig(i)=xlsread(loadstring,filename{i},'Y23');
deficit = vcj(i) - vwav;
btv = vwav((xlab>=btstart(1))&(xlab<=btend(1)));
btavev(i)=mean(btv);
defave(i)= vcj(i) - btavev(i);
f=figure();
scatter(xlab,vwav,'filled','sizedata',64)
hold on
scatter(aves(1,i),aves(2,i),'filled','g','sizedata',64)
plot(bt,[btavev(i) btavev(i)],'LineWidth',1.5)
plot([0,6],vcjvec,'k','LineWidth',2)
plot(btstart,[-500,3000],'r--','LineWidth',1.5)
plot(btend,[-500,3000],'m--','LineWidth',1.5)
grid on
axis([0,6,1000,2600])
xlabel('Distance (m)','FontSize',24)
ylabel('Velocity (m/s)','FontSize',24)
fleg=legend('Velocity','Centered BT Average Vel.','BT Average Vel.'...
    ,'V_{CJ}','BT Start','BT End','Location','SouthEast');
set(fleg,'FontSize',14)
g=figure();
scatter(xlab,deficit./vcj(i),'filled','sizedata',64)
hold on
scatter(aves(1,i),(vcj(i)-aves(2,i))./vcj(i),'filled','g','sizedata',64)
```

```
plot(bt,[defave(i)/vcj(i) defave(i)/vcj(i)],'LineWidth',1.5)
plot(btstart,[-500,3000],'r--','LineWidth',1.5)
plot(btend,[-500,3000],'m--','LineWidth',1.5)
grid on
axis([0,6,-.1,.5])
xlabel('Distance (m)','FontSize',24)
ylabel('\Delta V_{loss} / V_{CJ}','FontSize',24)
fleg=legend('Velocity Deficit/ V_{CJ}',...
    'Centered BT Average Vel. Def / V_{CJ}','BT Average Vel. Deficit',...
    'BT Start','BT End','Location','NorthEast');
set(fleg,'FontSize',14)
cd Images
filen1=sprintf('veldef_%s.png',filename{i});
print(g,filen1,'-dpng', '-r300');
filen2=sprintf('vel_%s.png',filename{i});
print(f,filen2,'-dpng', '-r300');
cd ..
end
psiatm = (psig + 14.7)/14.7;
defaveund = defave./vcj;
defmids=(vcj-aves(2,:))./vcj;
f=figure();
scatter(psiatm(1:12),defaveund(1:12),'b','sizedata',64)
hold on
scatter(psiatm(13:19),defaveund(13:19),'r','sizedata',64)
scatter(psiatm(20:21),defaveund(20:21),'g','sizedata',64)
scatter(psiatm(1:12),defmids(1:12),'filled','b','sizedata',64)
scatter(psiatm(13:19),defmids(13:19),'filled','r','sizedata',64)
scatter(psiatm(20:21),defmids(20:21),'filled','g','sizedata',64)
xlabel('Pressure (atm)','FontSize',24)
ylabel('\Delta V_{loss} / V_{CJ}','FontSize',24)
legend('1CH_4+2O_2','1CH_4+4N_2O','1.5CH_4+4N_2O',...
    '1CH_4+2O_2 Cent. Ave.','1CH_4+4N_2O Cent. Ave.',...
    '1.5CH_4+4N_2O Cent. Ave.');
grid on
cd Images
filen1='velvp_all.png';
print(f,filen1,'-dpng', '-r300');
cd ..
[psig,sortindex]=sort(psig);
btavev=btavev(sortindex);
vcj=vcj(sortindex);
defave=defave(sortindex);
defaveund = defave./vcj;
f=figure();
scatter(psiatm,btavev,'filled','b','sizedata',64)
hold on
plot(psiatm,vcj,'k','LineWidth',2)
grid on
xlabel('Pressure (atm)','FontSize',24)
```

```
ylabel('Velocity (m/s)','FontSize',24)
fleg=legend('Velocity','V_{CJ}','Location','SouthEast');
set(fleg,'FontSize',14)
g=figure();
scatter(psiatm,defaveund,'filled','sizedata',64)
axis([1,5,0,.12])
grid on
xlabel('Pressure (atm)','FontSize',24)
ylabel('\Delta V_{loss} / V_{CJ}','FontSize',24)
fleg=legend('Velocity Deficit / V_{CJ}','Location','NorthEast');
set(fleg,'FontSize',14)
cd Images
filen1='veldefvp_stoich.png';
print(g,filen1,'-dpng', '-r300');
filen2='velvp_stoich.png';
print(f,filen2,'-dpng', '-r300');
cd ..
```

B.3 Velocity-Distance BTRA Batch Plot

```
clear all; close all; clc; set(0,'DefaultAxesFontSize',16)
%Shot sequence is 1920-1947, 1920, 1924 & 1928 resulted in no data
shots=[20:47]; nodata=[20,24,28];
%Remove no data shots
for j=1:length(nodata)
shots(shots==nodata(j))=[];
end
%Recreate titles as seen in excel document
for j=1:length(shots)
shotlist{j}=['HS19' num2str(shots(j))];
end
%Excel document title
excelfile='New BT Data.xlsx';
for j=1:length(shotlist)
    [data,textin]=xlsread(excelfile,shotlist{j},'S24:AB72');
    %locations of beginning and end of BT section
    btstart=[data(1,7) data(1,7)]; btend=[data(2,7) data(2,7)];
    %user defined axis system
    axishigh=data(1,8); axislow=data(2,8);
    [a,b]=size(data);
    %checking for mag and pressure data
    if b>8
        xlab_mags=data(7:end,1);
        vlab_mags=data(7:end,2);
        xlab_pres=data(7:end,8);
        vlab_pres=data(7:end,9);
        pres=1;
    else
        pres=0;
        xlab_mags=data(7:end,1);
        vlab_mags=data(7:end,2);
    end
    myfiguresize=[0, 0, 1440, 900];
    f = figure('Position',myfiguresize);
    scatter(xlab_mags,vlab_mags,'filled','b','sizedata',64)
    leg={'EM Probe Velocity'; 'BT Start'; 'BT End'};
    if pres~=0
       hold on
       scatter(xlab_pres,vlab_pres,'filled','d','r','sizedata',64)
       leg={'EM Probe Velocity'; 'PCB Velocity'; 'BT Start'; 'BT End'};
    end
    hold on
    plot(btstart,[0,3000],'g-.','LineWidth',2);
    plot(btend,[0,3000],'m-.','LineWidth',2);
    legend(leg,'FontSize',14,'Location','NorthWest');
    xlabel('Distance (m)'); ylabel('Velocity (m/s)');
```

```
    grid on
    grid minor
    title(sprintf('%s',shotlist{j}))
    axis([0 8 axislow axishigh]);
    set(gca,'xtick',[0:.5:8])
    set(gca,'ytick',[axislow:50:axishigh])
    cd VX_Images
    filen1=sprintf('%s_VX.png',shotlist{j});
    set(gcf,'PaperUnits','inches','PaperPosition',[0 0 11 8.5])
    print(f,filen1,'-dpng', '-r300');
    cd ..
    close all
end
```

Appendix C

BAFFLED-TUBE DETONATION LOG

Tube Configuration:

BTD01 - BTD02: 2-meter-SB, 2-meter-BT, 2-meter-SB
BTD03 - BTD28: 2-meter-SB, 2-meter-BT, 4-meter-SB

Sparking Mechanism:

BTD01 - BTD09: Magneto BTD10 - BTD028: Sparking Circuit

Table Column Explanations:

Pressure (psig) and Detonation (X/DET): Shows the gauge pressure at which a detonation took place (marked by DET) or did not take place (marked by X).

Name	**Date**	**Spark Plug Type**	**Theoretical V_{CJ} (m/s)**	**Experimental $\bar{V}v_{CJ}$ in BT (m/s)**	**Chemistry**	**Pressure (psig) and Detonation (X/DET)**	**Notes**
BTD01	03/08/16	Axial	N/A	N/A	$1CH_4 + 2O_2$	60 X, 30 X,15 X, 3 X, 0 X	Aborted, No data
BTD02	03/08/16	Axial	2390	2130	$1CH_4 + 2O_2$	60 X, 30 X, 15 X, 1 DET	
BTD03	03/09/16	Axial	2400	2200	$1CH_4 + 2O_2$	60 X, 30 X,15 X, 5 X, 3 DET	
BTD04	03/09/16	Gap	N/A	N/A	$1CH_4 + 2O_2$	30 X, 15 DET	No trigger
BTD05	03/09/16	Gap	N/A	N/A	$1CH_4 + 2O_2$	16 DET	No trigger
BTD06	03/09/16	Axial	2400	2130	$1CH_4 + 2O_2$	16 DET	
BTD07	03/10/16	Axial	2210	2000	$1CH_4 + 2O_2$	20 X, 15 X, 12 X, 10 DET	
BTD08	03/10/16	Axial	2410	2290	$1CH_4 + 2O_2$	20 X, 17 X, 13 DET	
BTD09	03/10/16	Axial	2390	1000	$1CH_4 + 2O_2 + 1CO_2$	1 DET	Possible Deflagration
BTD10	05/17/16	Gap	2410	2290	$1CH_4 + 2O_2$	50.4 DET	
BTD11	05/20/16	Gap	2220	2070	$1CH_4 + 2O_2$	40.2 DET	
BTD12	05/20/16	Gap	2420	2360	$1CH_4 + 2O_2$	30.1 DET	
BTD13	05/20/16	Gap	2220	2120	$1CH_4 + 2O_2$	20.0 DET	
BTD14	05/24/16	Gap	2420	2310	$1CH_4 + 2O_2$	14.7 DET	
BTD15	05/24/16	Gap	2420	2310	$1CH_4 + 2O_2$	9.9 DET	
BTD16	05/24/16	Gap	2430	2340	$1CH_4 + 2O_2$	4.9 DET	
BTD17	05/27/16	Gap	N/A	N/A	$2CH_4 + 4N_2O$	40.0 X, 34.9 X, 19.8 X, 10.9 X, 5.6 X, 2.9 X, 1.4 X	Aborted, No data
BTD18	05/27/16	Gap	2230	2150	$1CH_4 + 4N_2O$	50.5 DET	
BTD19	05/30/16	Gap	2340	2240	$1CH_4 + 4N_2O$	39.1 DET	
BTD20	05/30/16	Gap	2240	2190	$1CH_4 + 4N_2O$	29.8 DET	
BTD21	05/30/16	Gap	2440	2400	$1CH_4 + 4N_2O$	20.1 DET	
BTD22	05/31/16	Gap	2240	2200	$1CH_4 + 4N_2O$	14.1 DET	
BTD23	05/31/16	Gap	2450	2420	$1CH_4 + 4N_2O$	10.1 DET	
BTD24	05/31/16	Gap	2350	2330	$1CH_4 + 4N_2O$	5.0 DET	
BTD25	06/01/16	Gap	2460	2480	$1.5CH_4 + 4N_2O$	49.6 DET	
BTD26	06/01/16	Gap	N/A	N/A	$1.75CH_4 + 4N_2O$	39.9 X, 30.1 X, 19.9 X, 9.9 X, 1.9 X	Aborted, No data
BTD27	06/01/16	Gap	2250	2240	$1.5CH_4 + 4N_2O$	29.5 DET	
BTD28	06/01/16	Gap	2340	2240	$1.5CH_4 + 4N_2O$	9.4 DET	

Appendix D

VELOCITY DEFICIT PLOTS

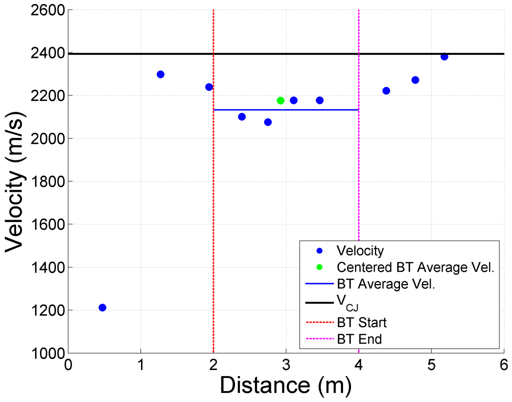

BTD02, $1CH_4+2O_2$, P_1=1 psig

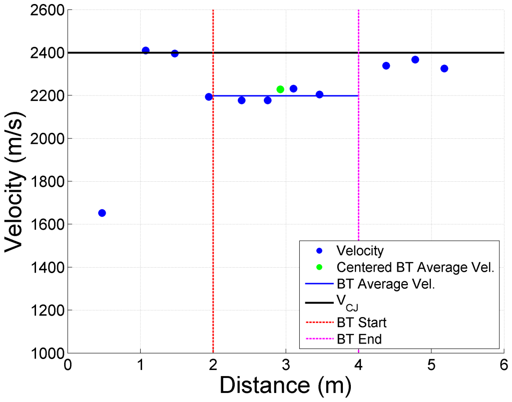

BTD03, $1CH_4+2O_2$, P_1=3 psig

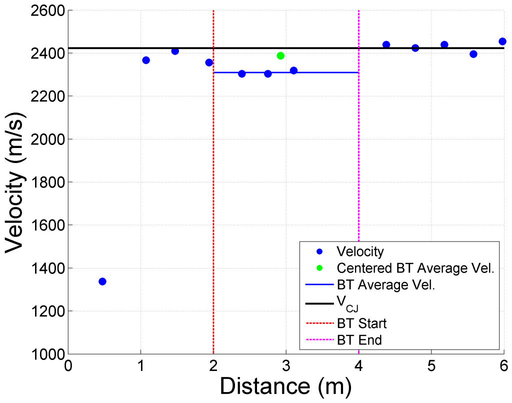

BTD06, $1CH_4+2O_2$, P_1=16 psig

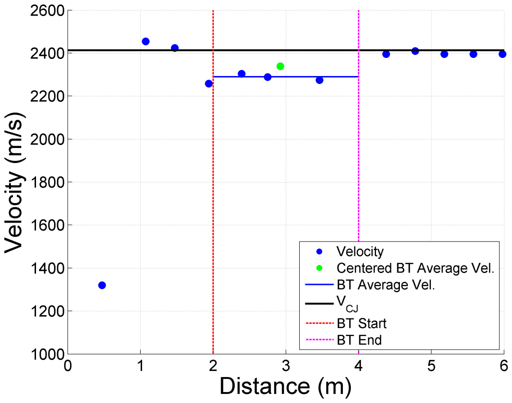

BTD07, $1CH_4+2O_2$, P_1=10 psig

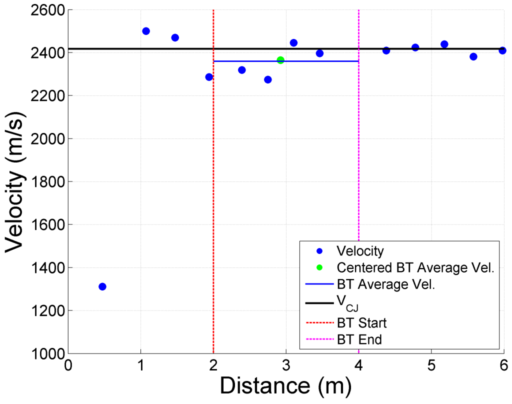

BTD08, $1CH_4$+$2O_2$, P_1=13 psig

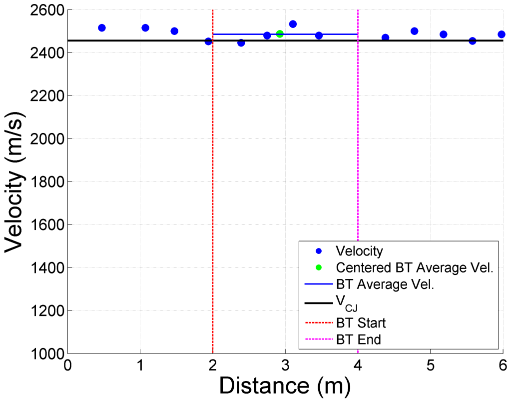

BTD10, $1CH_4$+$2O_2$, P_1=50 psig

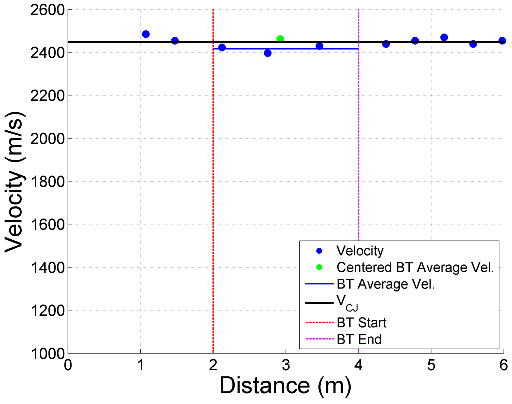

BTD11, $1CH_4$+$2O_2$, P_1=40 psig

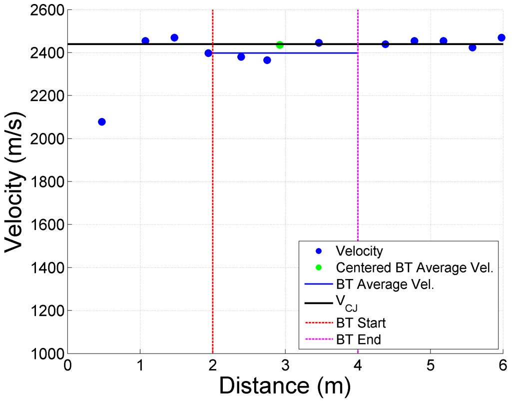

BTD12, $1CH_4$+$2O_2$, P_1=30 psig

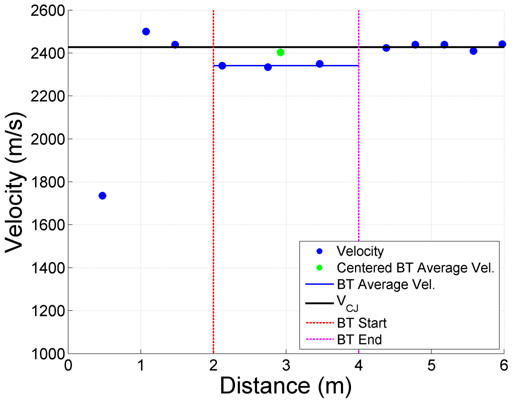

BTD13, $1CH_4$+$2O_2$, P_1=20 psig

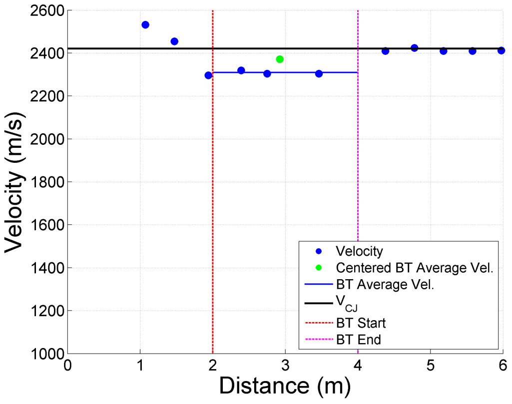

BTD14, $1CH_4$+$2O_2$, P_1=15 psig

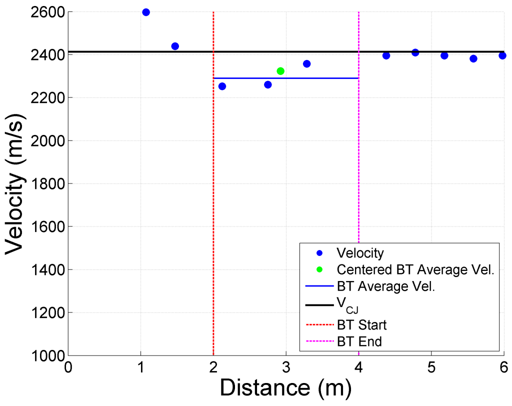

BTD15, $1CH_4+2O_2$, P_1=10 psig

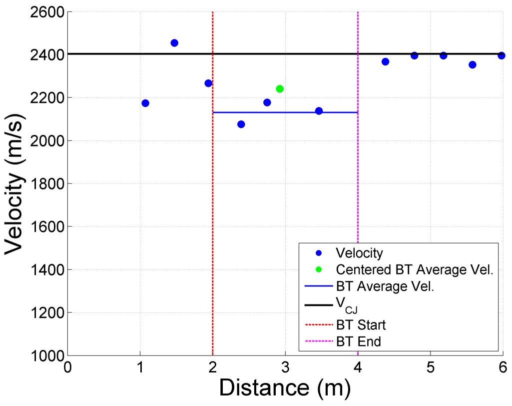

BTD16, $1CH_4+2O_2$, P_1=5 psig

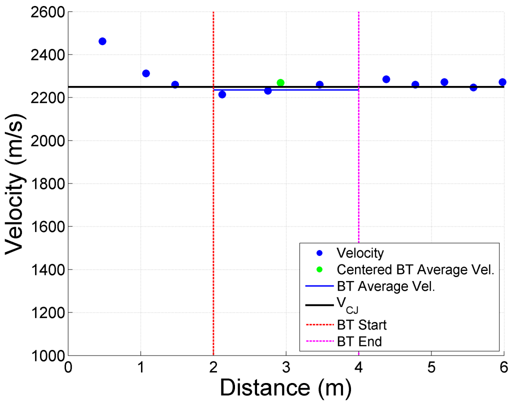

BTD18, $1CH_4+4N_2O$, P_1=51 psig

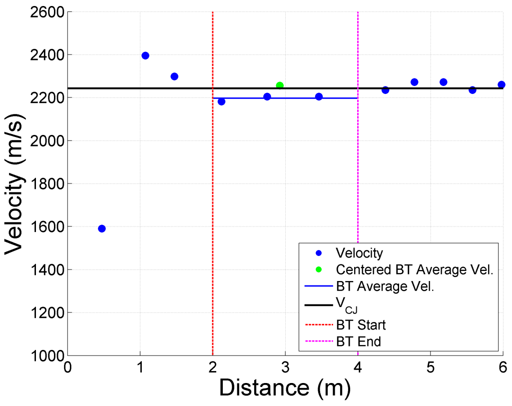

BTD19, $1CH_4+4N_2O$, P_1=39 psig

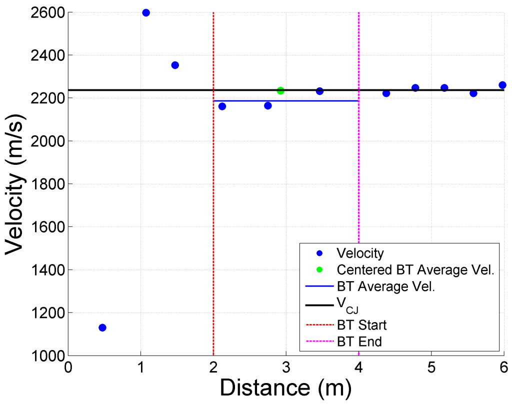

BTD20, $1CH_4+4N_2O$, P_1=30 psig

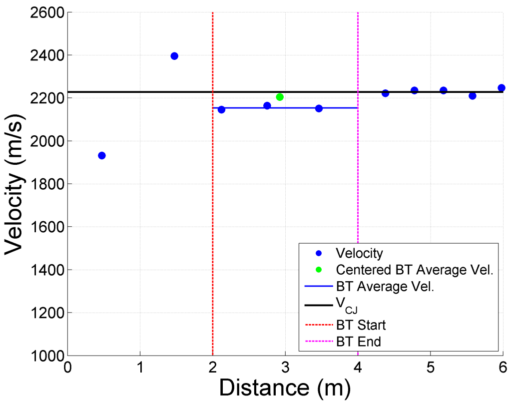

BTD21, $1CH_4+4N_2O$, P_1=20 psig

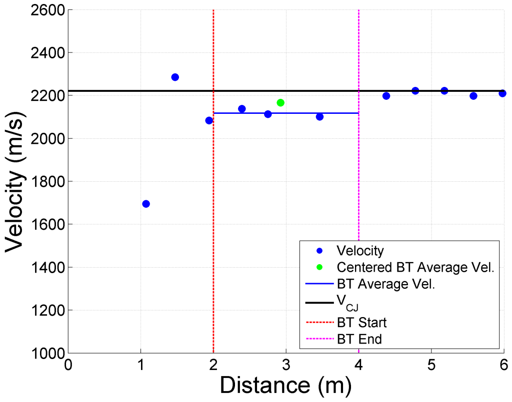

BTD22, $1CH_4+4N_2O$, P_1=14 psig

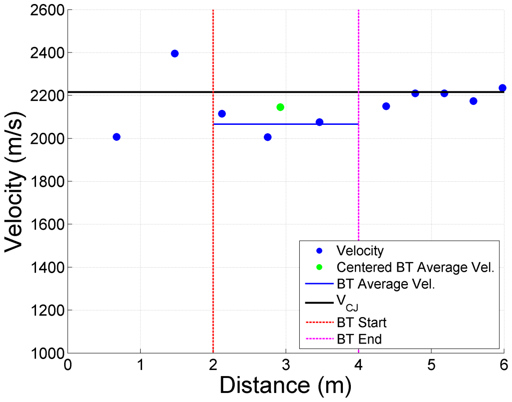

BTD23, $1CH_4+4N_2O$, P_1=10 psig

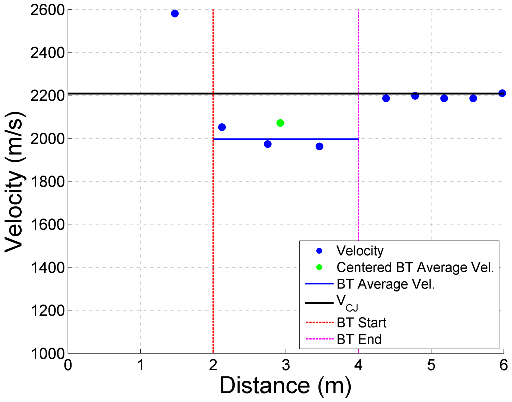

BTD24, $1CH_4+4N_2O$, P_1=5 psig

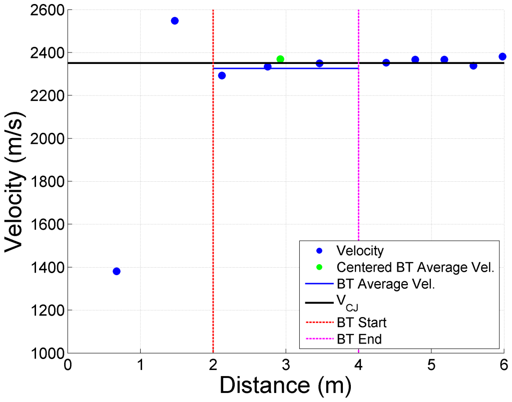

BTD25, $1.5CH_4+4N_2O$, P_1=51 psig

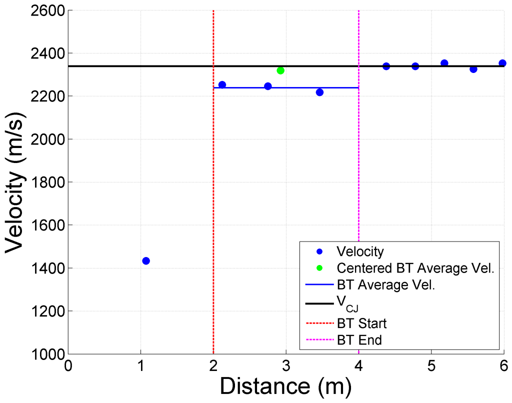

BTD27, $1.5CH_4+4N_2O$, P_1=30 psig

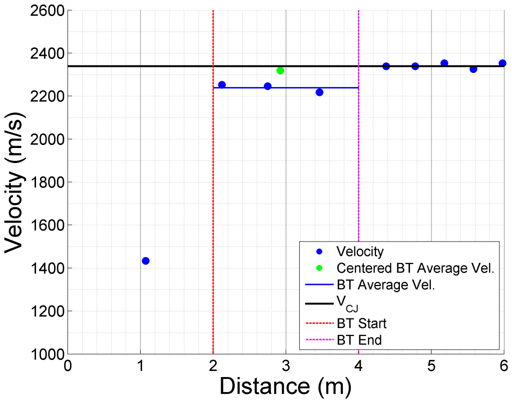

BTD28, $1.5CH_4+4N_2O$, P_1=10 psig

Appendix E

BAFFLED-TUBE RAM SHOT LOG

Table Column Explanations:

Projectile Configuration: Explains the type of projectile and obturator used with specified length and diameter measurements

Component Masses (grams): Component masses, P: Projectile (with mag installed) O: Obturator T: Total (after obturator adhered to projectile)

Breech Diaphragms: Shows the thicknesses of each diaphragm used, and the pressure in which it was scribed. Pattern is downstream / upstream, if only one diaphragm was used, it was placed in the upstream position and a blank was placed downstream.

Breech Pressures: Shows the fill pressures, pattern of breech pressure/bank pressure, if only one diaphragm was used, bank pressure is recorded.

Pressure Lengths: Shows the section fill pressures and their respective lengths in meters. All sections are marked from the beginning of the test section moving downstream until the last.

Name	**Date**	**Projectile Configuration**	**Comp. Masses (grams)**	**Comments**	**Breech Diaphragms**	**Breech Pres.**	**Fill Pres. (psig)**	**Entrance Velocity U_{in} (m/s)**	**ΔU in BT (m/s)**	**CJ Det. Vel. U_{CJ} (m/s)**	**Sound Speed a_0 (m/s)**	**Chemistry**	**Pressure Lengths**
HS1920	05/12/15	Lexan Axisymm. Annular Mag.	P: 151.59 O:16.97 T:168.67	No Shot Data	.064/.125 2300Ψ/3800Ψ	1010/4010	138	N/A	N/A	1500	294	$1CH_4+2O_2$ $+2.72CO_2$	VAC 1m 132 2m VAC 13m
HS1921	05/13/15	Lexan Axisymm. Annular Mag.	P: 154.10 O:16.00 T:170.12	Missing Breech O-ring	.064/.125 2300Ψ/3800Ψ	1060/3940	137	860	-5	1770	309	$1CH_4+2O_2$ $+2.72CO_2$	VAC 1m 131 2m 154 13m (N_2)
HS1922	05/15/15	Lexan Axisymm. Annular Mag.	P: 155.06 O:17.88 T:172.94		.064/.125 2300Ψ/3800Ψ	1110/4070	137	900	-150	1830	313	$1CH_4+2O_2$ $+2CO_2$	VAC 1m 132 2m 177 13m (N_2)
HS1924	05/26/15	Lexan Axisymm. Annular Mag.	P: 163.71 O:17.40 T:186.49	Prebroke diaphragm	.064/.125 2300Ψ/3800Ψ	1400/X	156	N/A	N/A	1830	313	$1CH_4+2O_2$ $+2CO_2$	VAC 1m 132 2m 189 13m (N_2)
HS1925	06/18/15		P: 146.73 O:29.89 T:176.76		.064x2/.125 2300Ψ/3800Ψ	2100/4250	135	950	-50	1770	309	$1CH_4+2O_2$ $+2.7CO_2$	VAC 1m 130 2m 192 13m (N_2)
HS1926	06/19/15	Lexan Axisymm. 2.901"L Long Obt. .745"L	P: 145.57 O:19.49 T:165.18		.064/.125 2300Ψ/3800Ψ	825/3750	138	900	150	1830	313	$1CH_4+2O_2$ $+2CO_2$	VAC 1m 130 2m 197 13m (N_2)
HS1927	06/22/15	Lexan Axisymm. 2.994"Lx1.468"$\oslash$ Obt. .755"Lx1.498"$\oslash$	P: 148.81 O:16.56 T:165.39		.064/.125 2300Ψ/3800Ψ	825/3720	137	910	40	1770	309	$1CH_4+2O_2$ $+2.35CO_2$	VAC 1m 130 2m 176 13m (N_2)
HS1928	06/23/15	Lexan Axisymm. 2.959"Lx1.464"$\oslash$ Obt. 1.497"$\oslash$	P: 147.17 O:22.98 T:170.26	Diaphragm Break, no shot	.064/.125 2300Ψ/3800Ψ	800/X	138	N/A	N/A	1860	314	$1CH_4+2O_2$ $+1.9CO_2$	VAC 1m 133 2m 196 13m (N_2)
HS1929	06/26/15	Lexan Axisymm. 3.020"Lx1.464"$\oslash$ Obt. 1.498"$\oslash$	P: 149.06 O:16.27 T:165.54		.125 3800Ψ	3000	138	850	125	1860	314	$1CH_4+2O_2$ $+1.9CO_2$	VAC 1m 133 2m 213 13m (N_2)
HS1930	06/30/15	1 pc. 9° tail 1.512"Lx1.465"$\oslash$	P:127.63 O:30.82 T:158.50		.125 3800Ψ	2925	138	850	50	1860	314	$1CH_4+2O_2$ $+1.9CO_2$	VAC 1m 133 2m 211 13m (N_2)
HS1931	06/30/15	1 pc. 9° tail 1.512"Lx1.465"$\oslash$	P:128.50 O:17.85 T:145.73		.064/.064 2300Ψ/2300Ψ	1025/2400	168	820	160	1860	314	$1CH_4+2O_2$ $+1.9CO_2$	VAC 1m 163 2m 0 3m (Air) 210 10m (N_2)
HS1932	07/01/15	2 pc. 20° tail 1.708"Lx1.469"$\oslash$ Annular Mag. Obt. 1.474"$\oslash$	P:145.72 O:19.84 T:162.30	Obt. Shattered	.064/.064 2300Ψ/2300Ψ	1170/2525	168	880	-80	1860	314	$1CH_4+2O_2$ $+1.9CO_2$	VAC 1m 164 2m 0 3m (Air) 224 10m (N_2)

Name	**Date**	**Projectile Configuration**	**Comp. Masses (grams)**	**Comments**	**Breech Diaphragms**	**Breech Pres.**	**Fill Pres. (psig)**	**Entrance Velocity U_{in} (m/s)**	**ΔU in BT (m/s)**	**CJ Det. Vel. U_{CJ} (m/s)**	**Sound Speed a_0 (m/s)**	**Chemistry**	**Pressure Lengths**
HS1933	07/01/15	2 pc. 20° tail 1.656”Lx1.470”⊘ Annular Mag. Obt. 1.474”⊘	P:143.72 O:16.31 T:159.99	Obt. Wall Shattered	.064/.064 2300Ψ/2300Ψ	800/2150	168	840	-100	1860	314	$1CH_4+2O_2$ $+1.9CO_2$	VAC 1m 164 2m 0 3m (Air) 230 10m (N_2)
HS1934	07/02/15	2 pc. 20° tail 1.742”Lx1.474”⊘ Annular Mag. Obt. 1.465”⊘	P:146.80 O:26.54 T:173.33	No break-up	.064/.064 2300Ψ/2300Ψ	670/1980	168	700	-110	1860	314	$1CH_4+2O_2$ $+1.9CO_2$	VAC 1m 163 2m 0 3m (Air) 225 10m (N_2)
HS1935	07/03/15	2 pc. 20° tail 1.768”Lx1.469”⊘ Annular Mag. Obt. 1.466”⊘	P:146.07 O:23.65 T:169.83	No break-up	.064/.064 2300Ψ/2300Ψ	650/2100	168	730	-110	1860	314	$1CH_4+2O_2$ $+1.9CO_2$	VAC 1m 163 2m 0 3m (Air) 205 10m (N_2)
HS1936	07/03/15	2 pc. 20° tail 1.701”Lx1.469”⊘ Annular Mag. Obt. 1.466”⊘	P:145.59 O:24.84 T:170.53	No break-up	.064/.064 2300Ψ/2300Ψ	1175/2600	168	790	150	1860	314	$1CH_4+2O_2$ $+1.9CO_2$	VAC 1m 163 2m 0 3m (Air) 197 10m (N_2)
HS1937	07/29/15	2 pc. 20° tail 1.699”Lx1.469”⊘ Annular Mag.	P:145.81 O:24.39 T:170.20		.125 3600Ψ	2950	138	840	70	2390	303	$2CH_4$ $+4N_2O$	VAC 2m 132 2m 0 2m (Air) 211 10m (CO_2)
HS1938	07/30/15	2 pc. 20° tail 1.664”Lx1.473”⊘ Annular Mag.	P:145.25 O:24.08 T:169.39		.125 3800Ψ	2840	138	840	-110	2380	296	$1.5CH_4$ $+4N_2O$	VAC 2m 138 2m 0 2m (Air) 211 8m (CO_2) VAC 2m
HS1939	08/10/15	2 pc. 20° tail 1.697”Lx1.470”⊘ Annular Mag.	P:145.74 O:23.81 T:169.36	Broke in half	.125 3800Ψ	2850	210	840	170	2390	303	$2CH_4$ $+4N_2O$	VAC 2m 207 2m 0 2m (Air) 215 8m (CO_2) VAC 2m
HS1940	08/11/15	1 pc. 9° tail 2.928”Lx1.465”⊘ Cylinder Mag.	P:145.60 O:24.48 T:170.08		.125 3800Ψ	2800	210	830	-220	2390	303	$2CH_4$ $+4N_2O$	VAC 2m 208 2m 0 2m (Air) 217 8m (CO_2) VAC 2m
HS1941	08/13/15	1 pc. 12° tail 2.287”Lx1.465”⊘ Cylinder Mag.	P:139.36 O:24.94 T:164.48		.125 3800Ψ	2750	210	850	230	2390	303	$2CH_4$ $+4N_2O$	VAC 2m 207 2m 0 2m (Air) 234 8m (CO_2) VAC 2m

Name	**Date**	**Projectile Configuration**	**Comp. Masses (grams)**	**Comments**	**Breech Diaphragms**	**Breech Pres.**	**Fill Pres. (psig)**	**Entrance Velocity U_{in} (m/s)**	**ΔU in BT (m/s)**	**CJ Det. Vel. U_{CJ} (m/s)**	**Sound Speed a_0 (m/s)**	**Chemistry**	**Pressure Lengths**
HS1942	08/13/15	1 pc. 12° tail 2.326"Lx1.465"⊘ Cylinder Mag.	P:139.83 O:24.41 T:164.46	Broke in half	.125/.125 3800Ψ/3800Ψ	2500/5450	138	1040	110	2390	303	$2CH_4$ $+4N_2O$	VAC 2m 133 2m 0 2m (Air) 252 8m (CO_2) VAC 2m
HS1943	08/14/15	1 pc. 12° tail 2.308"Lx1.465"⊘ Cylinder Mag.	P:140.21 O:24.50 T:164.75	Broke in half	.125 3800Ψ	2800	296	840	230	2390	303	$2CH_4$ $+4N_2O$	VAC 2m 294 2m 0 2m (Air) 270 8m (CO_2) VAC 2m
HS1944	08/18/15	1 pc. 12° tail 2.298"Lx1.465"⊘ Cylinder Mag.	P:139.49 O:24.80 T:164.46	Broke in half	.125/.125 3800Ψ/3800Ψ	2500/5550 H_2 970Ψ	210	1100	120	2390	303	$2CH_4$ $+4N_2O$	VAC 2m 208 2m 0 2m (Air) 288 8m (CO_2) VAC 2m
HS1945	08/20/15	1 pc. 12° tail 2.337"Lx1.464"⊘ Cylinder Mag.	P:139.85 O:24.11 T:164.026	Broke in half	.125/.125 3600Ψ/3600Ψ	2500/5450	138	730	210	2390	303	$2CH_4$ $+4N_2O$	VAC 2m 133 2m 0 2m (Air) 252 8m (CO_2) VAC 2m
HS1946	08/20/15	1 pc. 12° tail 2.307"Lx1.463"⊘ Cylinder Mag.	P:139.95 O:24.35 T:164.32		.064/.064 2300Ψ/2300Ψ	1000/1950	210	640	-200	2390	303	$2CH_4$ $+4N_2O$	VAC 2m 207 2m 0 2m (Air) 244 8m (CO_2) VAC 2m
HS1947	08/21/15	1 pc. 12° tail 2.297"Lx1.465"⊘ Cylinder Mag.	P:138.71 O:24.38 T:163.25	Broke tail off	.064/.064 2300Ψ/2300Ψ	800/1560	210	610	270	2390	303	$2CH_4$ $+4N_2O$	VAC 2m 208 2m 0 2m (Air) 245 8m (CO_2) VAC 2m

Appendix F

BTRA HOT-SHOT VELOCITY-DISTANCE PLOTS

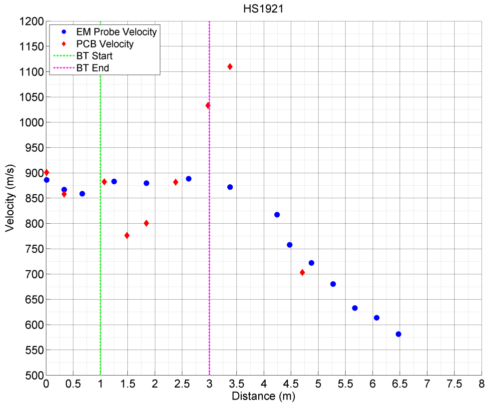

HS1921, $1CH_4+2O_2+2.7CO_2$, P_1=137 psig

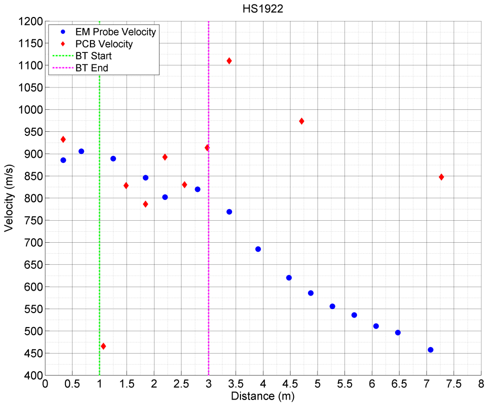

HS1922, $1CH_4+2O_2+2CO_2$, P_1=137 psig

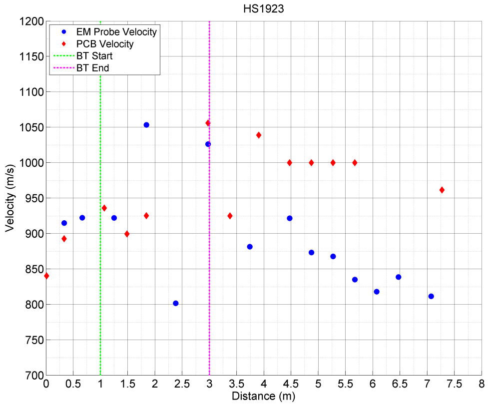

HS1923, $1CH_4+2O_2+2CO_2$, P_1=156 psig

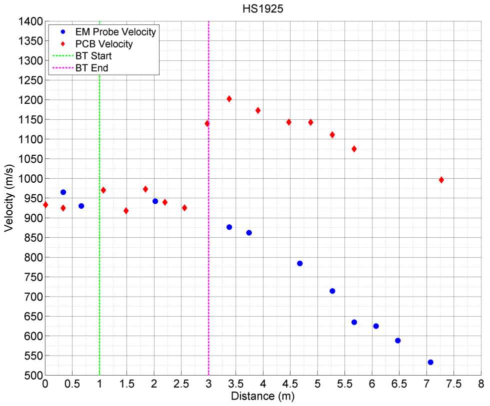

HS1925, $1CH_4+2O_2+2.7CO_2$, P_1=135 psig

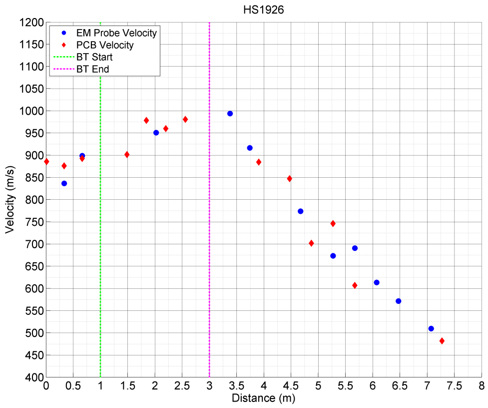

HS1926, $1CH_4+2O_2+2CO_2$, P_1=138 psig

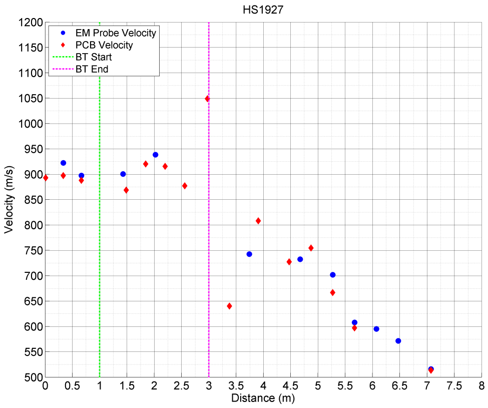

HS1927, $1CH_4+2O_2+2.4CO_2$, P_1=137 psig

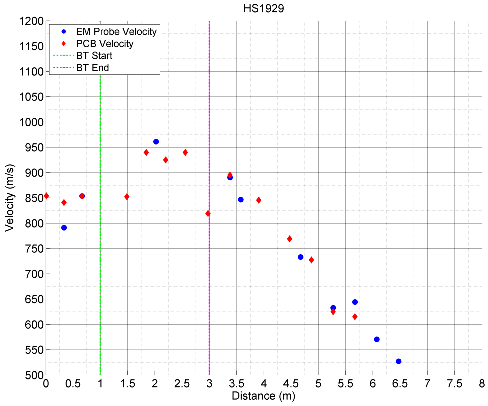

HS1929, $1CH_4+2O_2+1.9CO_2$, P_1=138 psig

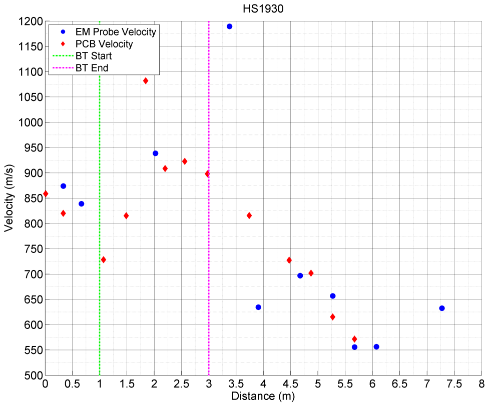

HS1930, $1CH_4+2O_2+1.9CO_2$, P_1=138 psig

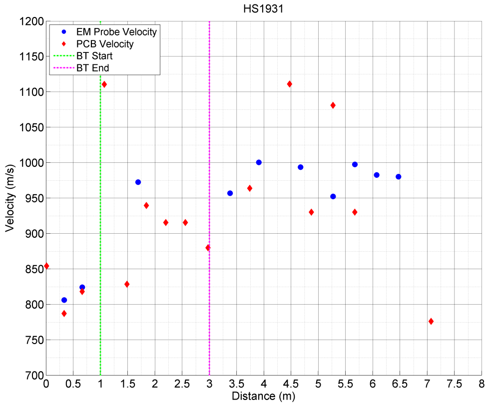

HS1931, $1CH_4+2O_2+1.9CO_2$, P_1=168 psig

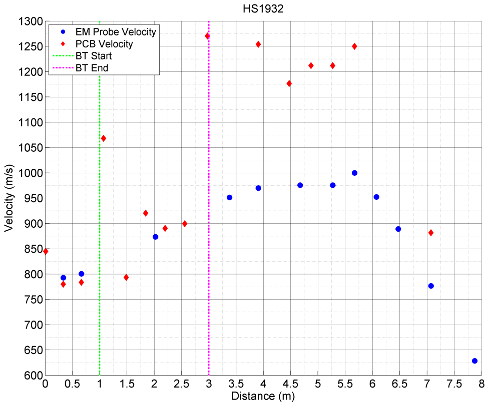

HS1932, $1CH_4+2O_2+1.9CO_2$, P_1=168 psig

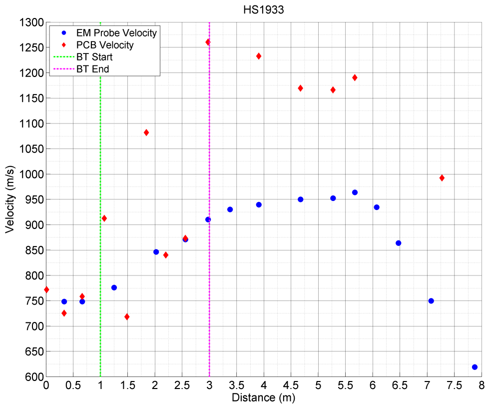

HS1933, $1CH_4+2O_2+1.9CO_2$, P_1=168 psig

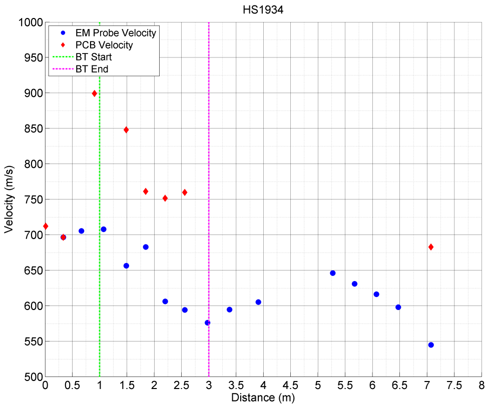

HS1934, $1CH_4+2O_2+1.9CO_2$, P_1=168 psig

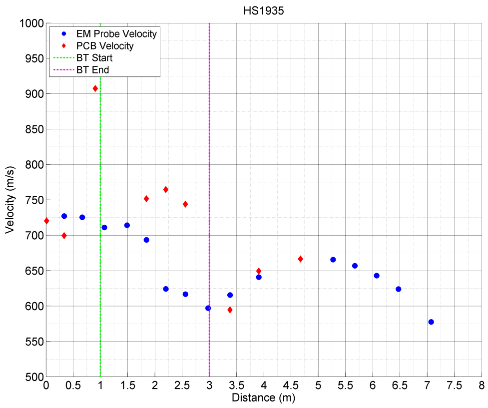

HS1935, $1CH_4+2O_2+1.9CO_2$, P_1=168 psig

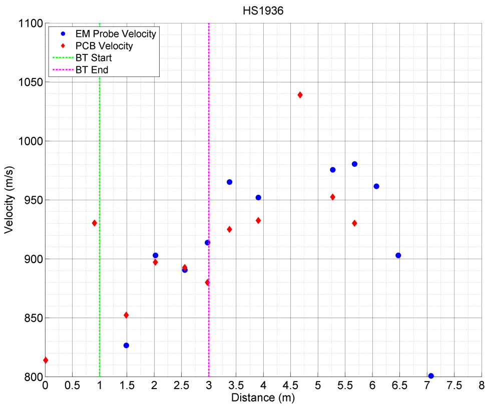

HS1936, $1CH_4+2O_2+1.9CO_2$, P_1=168 psig

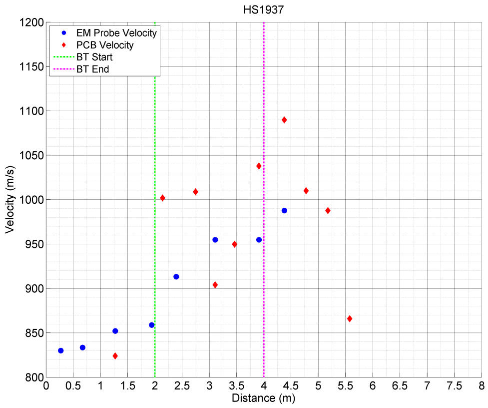

HS1937, $2CH_4+4N_2O$, P_1=138 psig

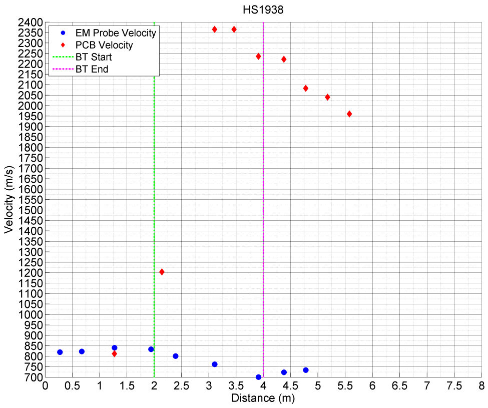

HS1938, $1.5CH_4+4N_2O$, P_1=138 psig

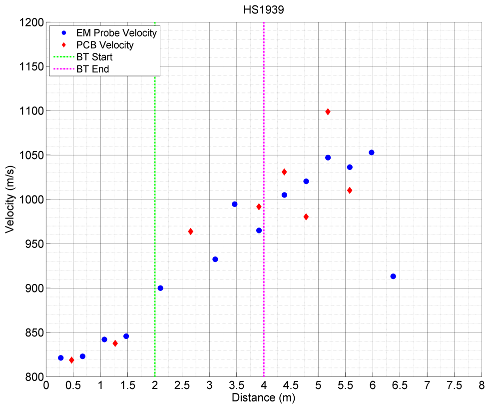

HS1939, $2CH_4+4N_2O$, P_1=210 psig

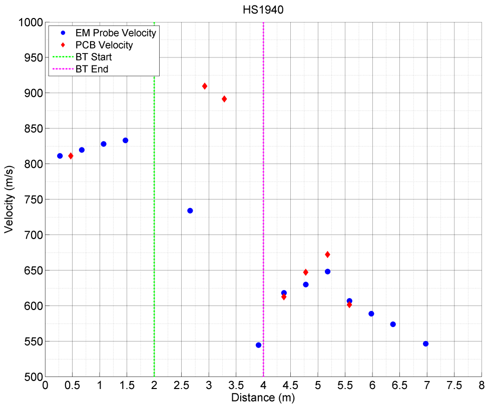

HS1940, $2CH_4+4N_2O$, P_1=210 psig

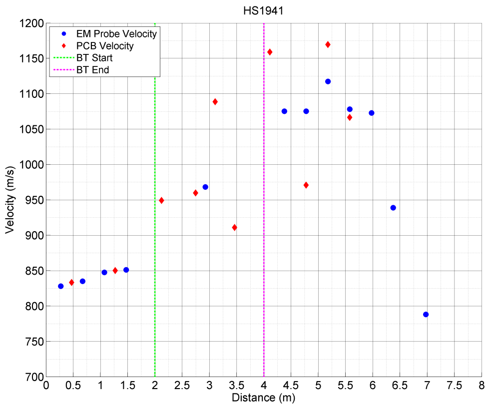

HS1941, $2CH_4+4N_2O$, P_1=210 psig

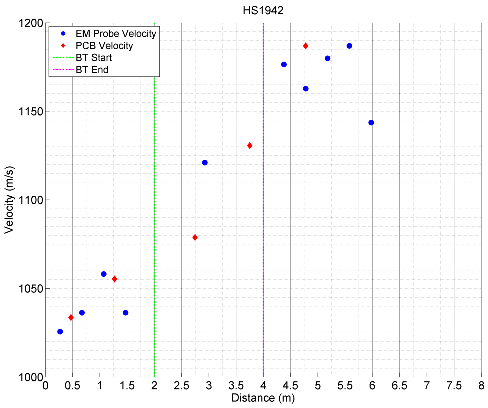

HS1942, $2CH_4+4N_2O$, P_1=138 psig

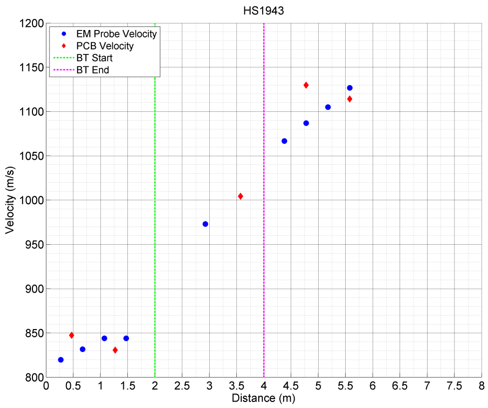

HS1943, $2CH_4+4N_2O$, P_1=296 psig

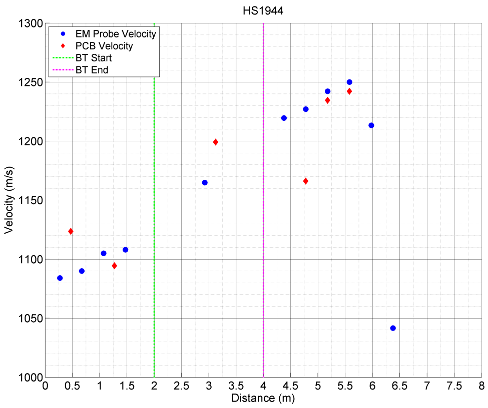

HS1944, $2CH_4+4N_2O$, P_1=210 psig

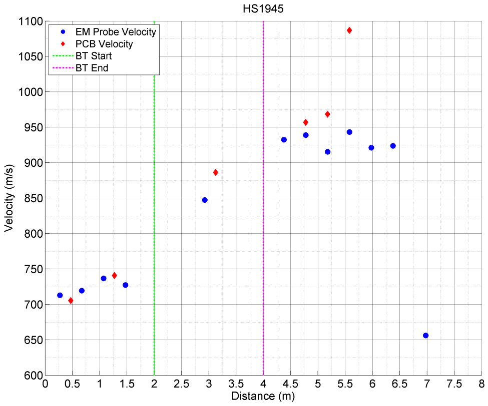

HS1945, $2CH_4+4N_2O$, P_1=138 psig

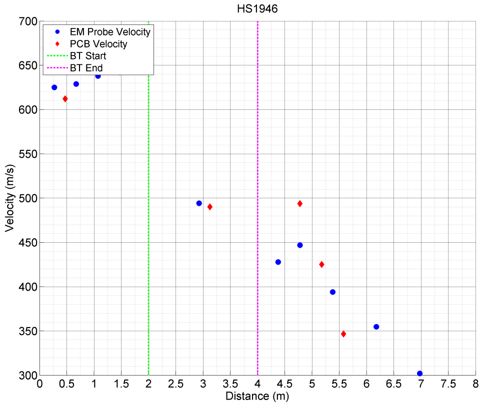

HS1946, $2CH_4+4N_2O$, P_1=210 psig

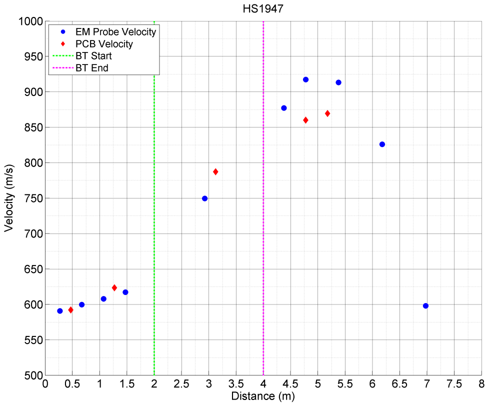

HS1947, $2CH_4+4N_2O$, P_1=210 psig